UCLouvain

epl

École polytechnique de Louvain

Hydrogen-Fueled Rotary Engine

Prediction and analysis of nitric oxide emissions

Author: **Louis Gouders**
Supervisor: **Pr. Francesco Contino**
Readers: **Pr. Hervé Jeanmart, Mauro Daese**
Academic year 2023–2024
Master [120] in Mechanical Engineering

Abstract

This research adapts the Homogeneous Two-Zone Finite Heat Release cycle for hydrogen-fueled rotary engines to predict nitric oxide (NO) emissions. This engine uses the rotational movement of a rotor to execute the four steps of internal combustion engine cycle. The simulation provides good agreement with literature and great understanding about the parameters involved in the variation of emissions such as air-fuel mixture, start of combustion, engine speed, ... However, the simulation could predict higher NO emissions than measured in future experiments due to assumptions and lack of study in rotary engine, especially concerning heat losses, influencing deeply the results.

Acknowledgement

I would like to begin by expressing my gratitude to Mr. Mauro Daese for his assistance throughout the development of this project. His experience and availability have been essential in the development of this thesis. His comments throughout the year enabled me to critique my work and achieve a high standard.

A great deal of gratitude is owed to my supervisor, Professor Francesco Contino. Firstly, for entrusting me with this project. Secondly, for his attentive listening, allowing me to feel the confidence he placed in my abilities. Thirdly, for granting me the freedom to choose a topic of study that is close to my heart, enabling me to conclude my studies on a subject that matters deeply to me. And finally, for his regular guidance and constructive criticism on my work, providing me with a rigorous framework. I would also like to thank Professor Hervé Jeanmart, not only as a reader but also as a participant in my evaluation committee.

I would like to thank the staff of the Catholic University of Louvain for their crucial assistance. Firstly, the technical staff of CREDEM: Pr. Herman, Arnaud, Frank, Hervé, Julien, Simon and Vincent for their time spent assisting me on this project and for sharing their deep knowledge, which has been invaluable. Additionally, I thank all individuals involved in parts procurement services for their assistance, time, and patience, especially Ms. Leduc.

Furthermore, I would like to express my gratitude to the community of automotive enthusiasts, comprising both professionals and hobbyists, for their interest in my project, for sharing their knowledge, and for their availability to respond to my questions.

Finally, I would like to thank my friends and family for their support during this writing process and throughout my academic journey at the university.

Contents

List of Figures

List of Tables

Nomenclature

Abbreviation

AF	Air-fuel ratio
AF_{st}	Stoichiometric air-fuel ratio
BDC	Bottom dead center
BHP	Brake horse power
CAS	Crank angle sensor
CI	Compression ignition
ECU	Electronic control unit
HICE	Hydrogen internal combustion engine
HRE	Hydrogen rotary engine
ICE	Internal combustion engine
IMEP	Indicated mean effective pressure
LHV	Lower heating value
NSU	Neckarsulm Strickmaschinen Union
OMP	Oil metering pump

P&ID	Piping and instrumentation diagram
RE	Rotary engine
RPM	Revolution per minute
SI	Spark ignition
TDC	Top dead center
LS	Leading spark
TS	Trailing spark
WRE	Wankel rotary engine

Symbols

A	Area
c	Concentration
C_p, C_v	Heat capacity (constant pressure and volume)
d	Characteristic length
e	Eccentricity
f	Residual fraction
h_c	Woschni convective heat transfer coefficient
H	Enthalpy
J	Jacobian
K_e	Equilibrium constant
$K_{(f,r)}$	Rate coefficient (forward, reverse)

m	Mass
$\dot{m}$	Mass flow
M	Molecular weight
p	Pressure
p_m	Motoring pressure
Q	Heat released
Q_l	Heat losses
Q_{in}	Combustion heat
R	Generating radius
R_u	Universal gas constant
S_L	Laminar flame speed
t	Time
T	Temperature
T_w	Wall temperature
U	Internal energy
V	Volume
V_s	Displacement
w	Mean gas velocity
W	Work
x	Mass fraction burned

y Molar fraction

Greek letters

α Ratio of nitric oxide concentration to its chemical equilibrium value

α_{th} Thermal diffusivity

γ Ratio of heat capacities

ν Stoichiometric coefficient

θ Crank angle

θ_d Crank angle burning timing

θ_s Crank angle start combustion

λ Excess air-fuel ratio

ρ Density

ϕ Equivalence ratio

ϕ_m Maximum angle of oscillation

$\dot{\omega}$ Rate of change of the molar concentration

Ω Engine speed

Introduction

Nowadays, due to the climatic crisis, engine manufacturers are searching for alternative fuels capable of reducing the carbon footprint of public transportation. While some are focusing their attention on electric alternatives such as batteries, others are considering the thermodynamic application of new fuel compositions. Amongst many combustibles considered, such as Methane, Ammonia, and Hydrogen, this last one is becoming increasingly popular among R&D departments.

Hydrogen is already used in aerospace facilities, and thanks to their research, many properties of this fuel are already known. As many other transportation sectors are starting their research, for example, the aeronautic sector with the new hydrogen propeller engine prototype announced by Airbus, it is time for the car manufacturing sector to increase their research on new fuel technologies. Some manufacturers are starting to announce their first prototypes of Hydrogen Internal Combustion Engine (HICE) cars, such as Mazda (2003), Toyota (2022) or even most recently Alpine with the *Alpenglow Hy4* in 2024.

The reason why hydrogen is increasingly appearing as an alternative fuel in ICE is not only due to its thermodynamic properties, which make it a great contender compared to the current fuels in use, but also due to its carbon footprint. Numerical simulations identify the combustion of pure hydrogen in ICE as a carbon-free process, and combined with the many possibilities to produce it (some of which can even make it close to carbon neutral), hydrogen could theoretically be one of the greatest solutions for sustainability. Unfortunately, some factors are not considered in numerical simulations, and the results can be slightly different in experimental applications. Current research focuses on understanding these variances to improve design.

Researchers have divided opinions on the purpose of hydrogen research and use. They are split between those looking at it as a recycling solution for reciprocating engines already on the market and those trying to understand its behaviour to make it the center of a next generation of ICE that could change car engine designs. The latter group is exploring applications on new designs, sometimes based on

older ones that the current market has banned for lack of performance or regulatory violations with carbon-based fuels.

This research first introduces the engine considered in the emission research program. This work aims to understand the use of hydrogen in rotary engines and its impact on pollutant emissions. Rotary engines were banned from the market due to emission issues and consumption, but their design could be a better contender for hydrogen use than reciprocating engines due to their unique properties. Next, it adapt an emission simulation model (primarily developed in the past for reciprocating engines using carbon-based fuels) to this application. This will help to understand the challenges in pollutant emissions for this engine. This numerical simulation follows many steps of improvement to obtain the most accurate prediction possible. After that, the laboratory process is explain in order to obtain data that can be used later to either compare with the simulations or improve its accuracy. Finally, an analysis of the results obtained in the numerical simulation is made to first compare the different steps of model improvement and then the impact of different engine parameters. At the end of this work, appendices do not only regroup the computations made during the model elaboration but also the data used for the thermodynamic properties issued, for example, from NASA's research programs, and the details of the test bench construction and the challenges encountered.

Chapter 1

Literature review

This literature review provides an in-depth exploration of hydrogen fuel as an alternative for rotary engines. To begin, an overview about internal combustion engines and the prevalent designs on the market followed by an introduction to the rotary engine, its history, and operational principles. Following, a synthesis about the properties of hydrogen fuel enables to understand its use and benefits for rotary engines. Finally, this chapter explains the environmental impact and the formation of nitric oxide gases concluded by the results and the observations made from existing simulation used to predict its emission for different fuels and engine design.

The objective of this chapter is to elucidate the significance of understanding the stakes involved and to provide fundamental knowledge essential for comprehending the development of numerical simulations of NO emissions in rotary engines.

1.1 Internal Combustion Engine

The first ICE uses the reciprocating motion of a piston to convert the chemical energy produced by the combustion of an air-fuel mixture into mechanical energy. The main characteristic of this engine is that the chemical energy propels the piston head into a linear motion, which is converted into rotational motion by the intermediate use of a connecting rod.

The combustion process, on the other hand, could differ depending on the type of fuel used. Indeed, fuel do not only needs an oxidizer to combust but also an energy source, internal or external depending on the fuel properties. For external energy sources, a device is needed to bring the air-fuel mixture to its ignition threshold energy. This is the case for spark ignition engines (SI), where the oxidizer and the

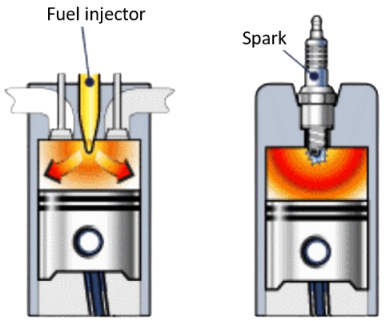

Figure 1.1: Compression (left) and spark (right) ignition process [26]

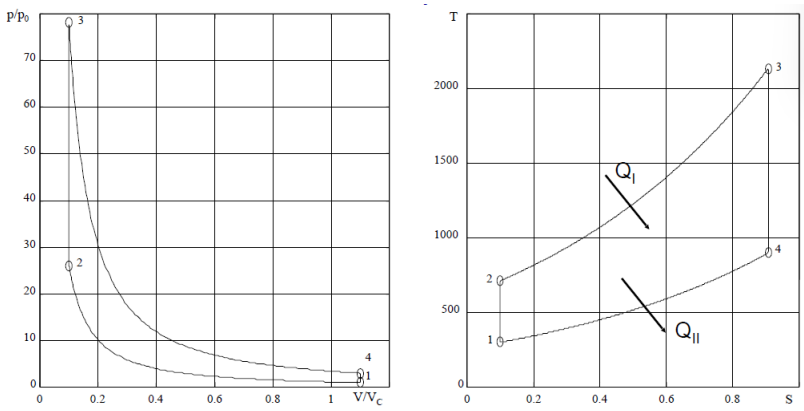

Figure 1.2: Evolution of the pressure and the temperature in *Beau de Rochas's* cycle [7]

fuel are premixed before a *spark* ignites the mixture. For internal energy sources, the fuel ignites by itself under specific pressure conditions. This method is used for compression ignition engines (CI), where the fuel is injected into highly compressed air. These two main designs are represented in Figure 1.1.

Internal combustion engines are designed to execute *Alphonse Beau de Rochas*'s four-step cycle [12], illustrated in Figure 1.2. Among the combustion designs, different engines differentiate themselves by the number of strokes needed to complete this cycle.

The four-stroke engine distributes each step of the cycle into four stroke of the piston, as illustrated in Figure 1.3. Two strokes are needed for the breathing phases (intake and exhaust), and two others for the mechanical strokes (compression and expansion). Each one is managed by the piston's linear motion in the cylinder, and additionally, the breathing strokes are possible due to the opening of the inlet and outlet valves driven by the camshaft.

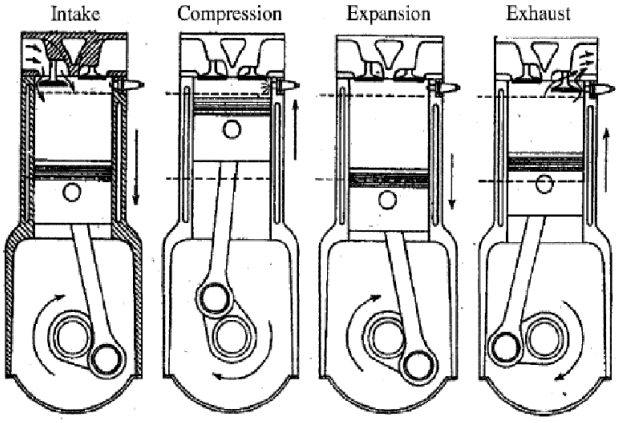

Figure 1.3: 4 strokes of a piston engine[**Fourstroke**]

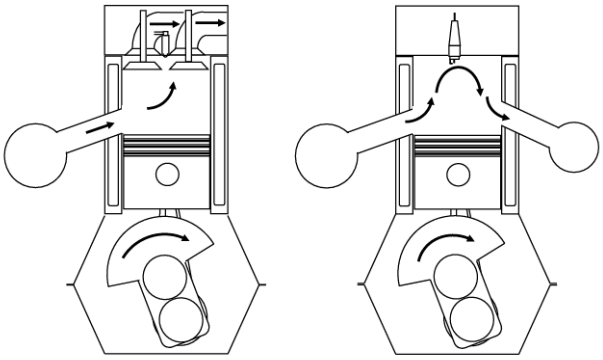

Figure 1.4: Two stroke engine scavenging methods[7]

During the full cycle, the crankshaft, responsible for transmitting power from the engine to its application, completes 720 degrees during the four strokes.

The two-stroke engine is designed to respond to specific applications where the four-stroke engine can not be applied, because of weight, size, or temperature restrictions. Indeed, the mechanical and breathing strokes are executed simultaneously. The piston's motion opens the breathing ports, inducing a scavenging process where the fresh mixture evacuates the dirty air according to two possible processes illustrated in Figure 1.4. By eliminating the valve system or downsizing it, the size of the engine and its complexity of synchronization are reduced.

1.2 Rotary Engine

1.2.1 History

Even though the reciprocating engine was then deeply integrated, many drawbacks such as vibration and weight due to the complex synchronization system led *Felix Wankel* to imagine his rotary compressor design as an internal combustion engine. The Wankel engine separates the four steps of the cycle as the four-stroke engine, but the breathing strokes use the two-stroke engine method by utilizing ports that are sealed and opened by the rotor's motion. Combining the port system and the rotational motion of the rotor, the Wankel engine is a much smaller and quieter engine capable to reach high speeds due to its rotational motion and the significant reduction of moving parts.

In *1954*, Felix Wankel developed the first *Wankel Rotary Engine* (WRE) for *NSU Motorenwerke* and conducted tests in *1957*. Subsequently, continuous efforts were made to create new designs capable of generating more power and reaching speeds around $25,000$ revolutions per minute (rpm).

Its production by NSU started in *1963*, powering the NSU Spider sports car. During the same period, numerous brands began developing their own variants under the Wankel license owned by NSU. Many of them, however, halted their research due to the engine's lack of performance compared to the research and development expenses. Nevertheless, one brand persisted in the development of this engine, making it their specialty.

In *1967*, *Mazda* introduced its first *rotary engine* (RE), powering the Cosmo 110S. From that point onwards, the brand continued producing cars equipped with this technology and designated this family of vehicles as the *RX* series.

The inaugural model, the *RX-2*, made its debut in 1970, paving the way for a series of subsequent models until 1978 when the most iconic car of the family emerged: the *RX-7*. Various iterations of this model were produced, including some equipped with a turbocharger, such as the RX7-FC illustrated in Figure 1.5, boosting the car's horsepower to over 200 (BHP). In *2003*, Mazda made a return with a sport car: the *RX-8*. The engine, named *Renesis*, was anticipated to be iconic. Regrettably, in *2012*, issues related to reliability and power losses compelled Mazda to cease the production of cars powered by rotary engines.

As the concept of rotary engines appeared to be fading, some engineers began recognizing the potential of rotary engines when powered by hydrogen. Despite initial apprehension, Mazda took a step forward by unveiling the *RX-E Hydrogen RE* as a prototype concept car in *2003*. Presently, Mazda is actively engaged in the

Figure 1.5: Mazda RX-7 FC

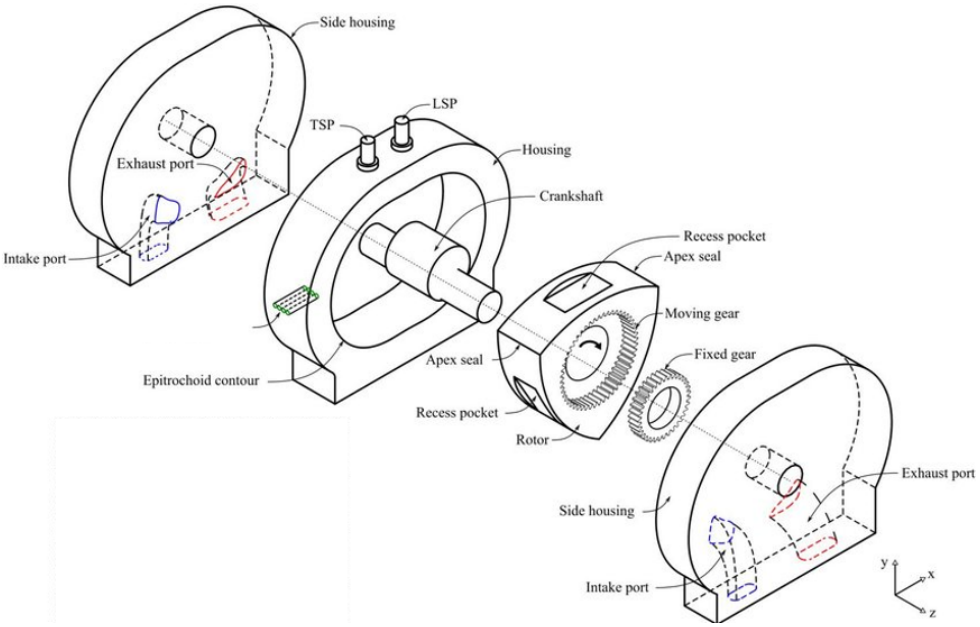

Figure 1.6: Wankel rotary engine design [22]

development of a new family of cars equipped with hydrogen rotary engines (HRE). This initiative reflects a renewed interest in the capabilities of rotary engines, now with a focus on utilizing hydrogen as a fuel source.

1.2.2 Engine cycle

As explained in Section 1.2.1, the RE was designed to address the shortcomings of the reciprocating engine. Therefore, the Wankel engine employs a rotor rotating within a housing, as illustrated in Figure 1.6. The rotational movement automatically opens and closes the two ports and allows the formation of three combustion chambers operating simultaneously.

Figure 1.7 illustrates the entire cycle of air in a rotary engine. Initially, air from the atmosphere enters the intake conduit (for atmospheric engines) or into the compressor (for turbocharged engines). Subsequently, based on the quantity of

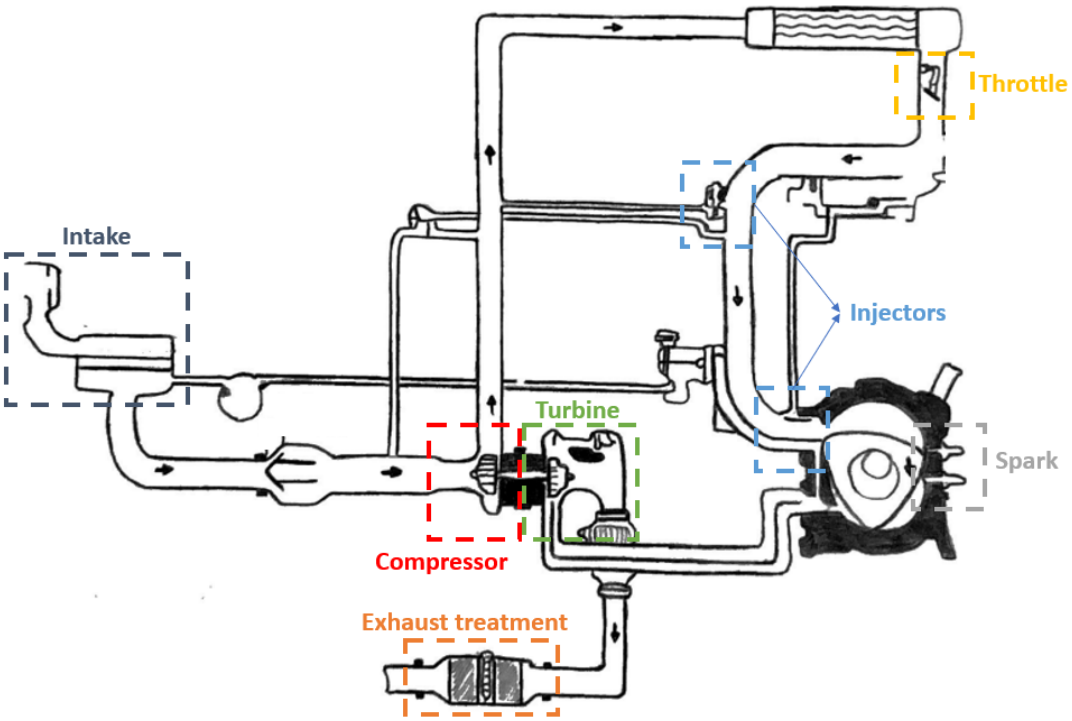

Figure 1.7: Air travel in the W.R.E.

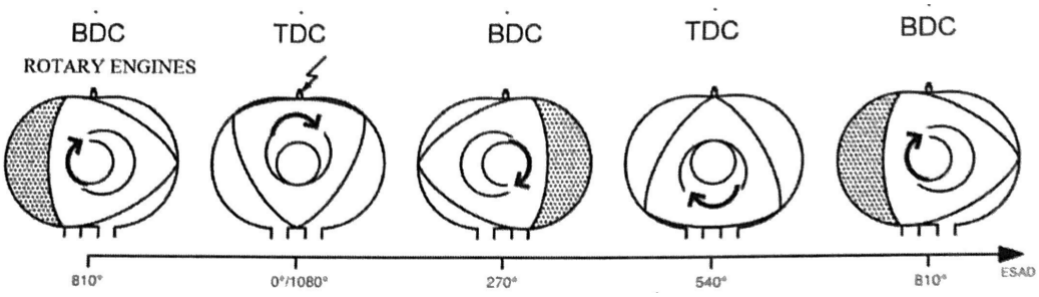

Figure 1.8: Full cycle of the rotor

air in the intake manifold and the speed of the engine, the electronic control unit (ECU) injects fuel to create a homogeneous mixture.

At the initiation of the rotor cycle, the intake port is open, allowing the gradual expansion of the chamber volume as the air-fuel mixture is drawn in. This expansion continues until reaching its maximum volume as known in reciprocating engine as bottom dead center (BDC) position. Following this, the mixture undergoes compression and is ignited close to its top dead center (TDC) position. Subsequently, the expansion process persists until reaching the second BDC position. Finally, the rotor opens the exhaust port, enabling the evacuation of the burned gases. This concise sequence outlines the key stages in the RE cycle.

All the described steps, illustrated in Figure 1.8, collectively contribute to the completion of the 1080 degrees of rotation of the crankshaft. Indeed, due to the unique triangular shape of the rotor, three combustion chambers can operate simultaneously. Consequently, after a full rotation of the rotor, three explosions occur. This implies that for every full rotation of the rotor, the output shaft (linked to the gearbox and the wheels) undergoes three rotations through the coupling mechanism between the moving gear and the fixed gear attached to the crankshaft, resulting in good torque fluctuation.

Finally, the burned gases are directed into the exhaust pipe, where they proceed to enter either the turbine (for turbocharged engines) or directly into the exhaust gas treatment system before being released into the atmosphere.

1.2.3 Drawbacks

Even though the rotary engine compensates for the defaults of piston engines, many automotive companies ceased production due to the significant drawbacks outweighing its benefits. The key disadvantages include:

Longer stroke: Longer presence of gases in the combustion chamber leads to a

quench effect where the hot gases come into contact with cooled chamber walls. This exposure extinguishes the flame and reduces combustion efficiency, but also increase pollutant formation such as hydrocarbons.

Burned oil: The rotor inside the housing is lubricated to ensure the long-term durability of the apex sealing shown in Figure 1.6. However, the presence of oil in the combustion chamber leads to impurities in the air-fuel mixture. These impurities are burned, leading to more carbonated gases and pollutant formation.

High fuel consumption: To achieve comparable output power to reciprocating engines, rotary engines need to run at higher speed. This requires more engine cycles and, thus, more fuel consumption compared to an equivalent displacement reciprocating engine.

Leakage: The challenge of isolating the three combustion chambers due to the complex motion of the rotor leads to significant gas leaks between chambers. These leaks reduce the combustion efficiency.

These challenges, coupled with advancements in piston engine technology and emission regulations complexity, prompted the discontinuation of rotary engine production by automotive manufacturers.

1.3 Hydrogen

1.3.1 Hydrogen fuel

Hydrogen is being more and more considered as fuel for the research of renewable solutions. However, hydrogen properties need to be understood before using it in ICE:

Range of flammability: Hydrogen has a wide range, allowing operation in extreme low or high concentrations within the air. This wide flammability range enables the management of pollutant concentrations and facilitates engine starting. For hydrogen, this range extends from 4 to 75% of the volume of the fuel-air mixture.

Ignition energy: 0.02 $[mJ]$ is sufficient to ignite hydrogen compared to 0.28 $[mJ]$ for gasoline fuels. Unfortunately, this means that hot spots or hot gases pose a risk of being energy sources high enough to ignite the gas.

Quenching distance: The quenching distance is the minimum distance between surfaces where the flame front extinguishes. With its 0.64 $[mm]$, Hydrogen has a greater tendency for backfire or blowby compared to the 3.5 $[mm]$ for

Properties	Hydrogen	Units
Molecular weight	2.016	g/mol
Density	0.08	kg/m^3
Minimum ignition energy required	0.02	mJ
Quenching distance	0.64	mm
Range of flammability	4-75	% of volume
Air-fuel ratio	34:1	kg_{air}/kg_{fuel}
Flame speed	290	cm/s
Auto-ignition temperature	584.85	$°C$
Air diffusivity	0.61	$[cm^2/s]$

Table 1.1: Synthesis of the proprieties of Hydrogen at atmospheric conditions (1 $[atm]$ and 300 $[K]$)

hydrocarbon fuels. Indeed, the smaller the quenching distance, the better the flame front can pass through narrow spaces.

Flame speed: The laminar flame speed of hydrogen approaching the 3 $[m/s]$ tends to almost seven times quicker than gasoline fuel with a flame speed approaching 0.4 $[m/s]$. It is important to note that while laminar flames are mainly observed during laboratory experiments, in reality, the flame is in turbulent regime where the speed is significantly higher.

Diffusivity: Hydrogen is highly diffusive in air, providing two main advantages: a uniform mixture and, in case of leaks, quick dispersion in the atmosphere, limiting dangerous concentrations and the possibility of burning.

Auto-ignition: Hydrogen auto-ignition temperature is very high making it complex to reach under only compression giving it a proper advantage for knock risks.

1.3.2 Hydrogen Rotary Engine

Hydrogen, used as fuel, offers many advantages. First, its combustion reduces the production of carbon-based substances, which are mainly due to the presence of lubricating oil in the combustion chamber or carbon compounds in the intake air. Second, its wide range of flammability also contributes to reducing pollutant emissions, as the fresh gas mixture entering the combustion chamber can achieve very lean or rich mixtures. These parameters influencing the reduction of carbon-based substances make hydrogen a strong contender for combating the greenhouse effect and global warming caused by the transportation sector. Finally, its high auto-ignition temperature decreases the risk of knocking, thereby protecting the

engine.

These features benefit all kinds of internal combustion engines (ICE), especially in addressing the main drawbacks of rotary engines concerning fuel consumption and pollutant emissions. Although the use of hydrogen in ICE poses multiple challenges, the characteristics of the rotary engine could make it better competitor.

Pollutant emissions The reduction of carbon molecules emissions leads to an increase in nitrogen oxides (NOx), which are also pollutants. However, NOx are mainly caused by high temperatures. Therefore, the longer exposure of burned gases to cooled walls makes rotary engines emit fewer nitrogen oxides than reciprocating engines [11] [17] [8].

Backfiring a major risk for reciprocating engines because the four strokes operate in the same volume, exposing the fresh gases to hot spots at the beginning of the intake stroke. In rotary engines, the four strokes are exposed to separate areas, leading to an inconsistent in-wall temperature distribution. In RE, the fresh gases are exposed to hot spots after the intake stroke, reducing the risk of backfiring. Additionally, the longer strokes expose the hot gases to more cooled surfaces, significantly reducing hot spot exposure and burned gas temperature.

Ignition timing The high-speed flame propagation properties of hydrogen allow for a reduction in the advancement of ignition timing. As the engine speed is typically limited by the slow combustion speed of carbon-based fuels because of the risk of backfiring. When using hydrogen, the ignition timing can be significantly delayed, further protecting the fresh gases from backfiring and increasing the maximum in-wall temperature later in the engine cycle.

These theoretical features make this engine a strong candidate for the development of hydrogen internal combustion engines.

1.4 Nitrogen oxides

Nitrogen oxides, commonly known as NOx, are one of the many pollutants present in the smokes of internal combustion engines. The other pollutants, considered as carbonated or sulfurized gases, are not produced in hydrogen combustion, theoretically. Nitric oxide (NO) is the base molecule of this category and results from the oxidation of nitrogen initially present in the oxidizer and/or the fuel, resulting in the combustion products. Upon release into the atmosphere, it further reacts to form the other gases listed in Table 1.2. Together, they contribute to environmental issues such as acid rain and the greenhouse effect.

Structure	Name
NO_3	Radical nitrate
N_2O_5	Dinitrogen pentoxide
NO_2	Nitrogen dioxide
N_2O_4	Trinitramide
N_2O_3	Dinitrogen tetraoxide
$N(NO_2)_3$	Dinitrogen trioxide
NO	Nitric oxide
N_2O_2	Dinitrogen dioxide
N_2O	Nitrogen monoxide
NO_2N_3	Nitryl azide
NON_3	Nitrosyl azide

Table 1.2: NO_x gases [27]

1.4.1 Sources

The formation of nitric oxide is due to the presence of nitrogen and oxygen in the combustion products. Despite the multiple considerations of nitrogen as an inert gas. In high temperature and kinetic conditions the high energized bonds between the nitrogen molecules (944 $[kJ/mol)$ [5] tend to brake and react with oxygen. There are three possibilities of the formation of NO which depend on the source of nitrogen.

Nitrogen in fuel: N_2 can be present in the fuel (for example, Nitromethane). At this point, the quantity of N_2 contained in the combustible depends on its nature. In that case, it is called *fuel nitrogen* and it is one of the biggest sources of nitric oxide formation. [25][3]

Nitrogen in air: The oxidizer could also be the source of N_2 such as air commonly used and approximately composed of 79% of it. The *Prompt mechanism* corresponds to the reaction between the nitrogen and the hydrocarbon radicals in the products. Then, the products resulting from the general equation 1.1 oxidize in the flame to create NO.

$$CH_x \ + \ N_2 \rightarrow \nu_\alpha \ H_u C_v N_w \tag{1.1}$$

The *Thermal mechanism*, the second possible reaction, is characterized by the reaction between oxygen and nitrogen.

$$N_2 \ + \ O_2 \rightarrow 2 \ NO \tag{1.2}$$

Among all three mechanisms, only the thermal mechanism is to be considered in

pure hydrogen combustion. Therefore, it is important to identify the parameters and conditions where the reaction occurs.

1.4.2 Thermal mechanism

As a reminder, to initiate a reaction, molecules need enough energy divided by two components in order to break and create new molecular bonds :

The internal energy of molecules is driven by the temperature diffusion which increases the molecule vibration and thus its microscopic velocity.

The kinetic energy driven by the mass diffusion during the mixture of the reactants influencing the mean particle velocity.

Because the mass diffusion is govern by the turbulence created by the rotor within the housing, only temperature can be managed to influence the reaction of nitrogen molecules in addition with the excess oxygen molecules resulting from the combustion of pure hydrogen.

In order to limit the production of NO, the energy of the molecule has to be limited. The microscopic velocity is the only one that can be downsized because the mean velocity is related to the motion of the gases in the chamber. In order to identify the temperature threshold, *Zeldovich* published the chain reaction creating the nitric oxide gases that has been completed by Lavoie, Et al in 1970. [15]

$$\begin{aligned} N_2 + O &\leftrightarrow NO + N \\ O_2 + N &\leftrightarrow NO + O \\ OH + N &\leftrightarrow NO + H \end{aligned}$$

This model is an approximation of the formation process. The threshold temperature identified where NO are starting to form is around 1400 $[K]$, grows exponentially as the temperature is rising reaching its maximum at 1900 $[K]$ and is dissociated for temperature between 2400 $[K]$ and 6200 $[K]$ according to research made by K. Thielen and P. Roth. [4][24]

Set aside the concentration of molecules resulting from the combustion needed for the reaction to occur, temperature is the major factor for the formation process. But the quantity of nitric oxide produced also depends on the *residence time*, which indicates the amount of time where the products are exposed to ideal formation conditions.

1.4.3 Emissions research

Many studies have been conducted to estimate the NO concentration in different ICE designs considering various fuel use. Over the years, simulation models have evolved from single-zone models, where researchers computed the mean states in the combustion chamber, to multiple-zone models capable to simulate the combustion process, allowing for a better representation of chemical kinetics. However, one of the most commonly used is the Homogeneous Two-Zone Finite Heat Release (HTZ) cycle, introduced notably in [3]. This model has been verified and used for simulating performance and emissions in reciprocating engines. However, adapting it for rotary engines has proven more challenging due to their unconventional properties, such as geometry and kinetics. While the HTZ model provides a great understanding of NO formation, its application to rotary engines from Ferguson, Et al in 1974 has shown a net overestimation of nitric oxide concentrations. This is mainly due to the lack of studies addressing the complexity of the engine, sometimes predicting almost an order of magnitude above measurements for gasoline applications at their time. [8]

On the other hand, experiments concerning NOx have been conducted on reciprocating engines using hydrogen. As expected, the concentration of nitric oxide has been observed to be much higher, almost twice as much, in the experiments conducted by Sun, Duan, and Liu (2014), with peaks sometimes exceeding 9000 $[ppm]$ [1].

Chapter 2

Numerical methodology

This chapter consolidates the complete mathematical approach to predict the concentration of nitric oxide in exhaust gases during the compression and expansion phase for one rotor. The development of the equations is detailed and then translated into programming code using the Python programming language (link in Appendix A.3) and the thermodynamic properties listed in Appendix B.

To begin, this chapter develops the Zeldovich model. Next, the numerical methodology proposes different models introduced in [3] for reciprocating engines adapted to the case study. These computations estimate the evolution of the states. Starting by introducing the Finite Energy Release model to understand the basic computations used to predict the evolution of engine states, subsequently, this chapter further develop this model with the Homogeneous Two-zones Finite Heat Release cycle, which is more accurate and relevant for this application.

Finally, this chapter delves more deeply into the parameters of the equations that need to be modified to fit rotary engines application followed by an identification and explanation of the different factors relevant to analyse.

2.1 Nitric oxide prediction

The Zeldovich model implies to identify the quantity of molecules produced by the combustion of hydrogen. As the general combustion process produces generally water molecules and nitrogen, in reality, the high temperatures dissociates the molecules producing more diversified products at equilibrium,[3][9]

$$\begin{aligned}\nu_f H_2 + \nu_a(O_2 + 3.76N_2) \longrightarrow & \nu_1 H_2O + \nu_2 N_2 + \nu_3 O_2 + \nu_4 H_2 \\ & + \nu_4 H_2 + \nu_5 H + \nu_6 O + \nu_7 OH + \nu_8 NO\end{aligned} \tag{2.1}$$

$$N_2 + O \overset{K_1}{\longleftrightarrow} NO + N \tag{2.2}$$

$$O_2 + N \overset{K_2}{\longleftrightarrow} NO + O \tag{2.3}$$

$$OH + N \overset{K_3}{\longleftrightarrow} NO + H \tag{2.4}$$

With the rate of reactions equation for these reactions, K_i, obtain experimentally, [3] [20]

$$K_{1f} = 1.8 * 10^{14} \exp \frac{-38370}{T} \qquad K_{1r} = 3.8 * 10^{13} \exp \frac{-425}{T} \tag{2.5}$$

$$K_{2f} = 1.8 * 10^{10} T \exp \frac{-4680}{T} \qquad K_{2r} = 3.8 * 10^{9} \exp \frac{-20820}{T} \tag{2.6}$$

$$K_{3f} = 7.1 * 10^{13} \exp \frac{450}{T} \qquad K_{3r} = 1.7 * 10^{14} \exp \frac{-24560}{T} \tag{2.7}$$

the expression for nitric oxide becomes,

$$\begin{aligned} \dot{\omega}_{NO} =& K_{1f} c_O c_{N_2} - K_{1r} c_{NO} c_N + K_{2f} c_N c_{O_2} \\ & - K_{2r} c_{NO} c_O + K_{3f} c_N c_{OH} - K_{3r} c_{NO} c_H \end{aligned} \tag{2.8}$$

There is a significant difference in the speed of reaction between these reactions. By observing the rate of changes, the second equation involved in NO formation is much more slower than the two others because K_2 is more than an order of magnitude lower than K_1 and K_3. Therefore, the *steady state approximation* can be applied because the concentration of the nitrogen radical is considered to be so fast that its rate of change is almost equal to zero. This helps to make (2.8) depend only on the concentrations of the products in (2.1),

$$\dot{\omega}_{NO} = 2(K_{1f} c_O c_{N_2} - K_{2r} c_{NO} c_O - K_{3r} c_{NO} c_H) \tag{2.9}$$

Further, the concentrations are computed according to the equilibrium composition of the combustion process further introduced in Section 2.3.2. The rate of change of nitric oxide becomes,[8] [3]

$$\dot{\omega}_{NO} = \frac{2R_1(1-\alpha^2)}{1 + \alpha R_1/(R_2 + R_3)} \tag{2.10}$$

Where,

- α is the ratio of nitric oxide concentration, $[NO]$ to its equilibrium value, $[NO_e]$
- R_i is the various rate of reaction with the equilibrium concentrations

Finally, the total amount of nitric oxide is computed by integrating the mass fraction computed across the charge after the NO levels are at equilibrium also called *frozen*, [8]

$$[NO] = \int_0^1 x_{NO} dx \times 10^6 \ [ppm] \tag{2.11}$$

2.2 Temperature distribution models

The two models introduced in this section are base on the differential energy equation for an open system,

$$\delta Q - \delta W = dU + \frac{\dot{m}_l h_l}{\omega} \tag{2.12}$$

Where :

- Q is the heat exchange $[kJ]$
- W is the work $[kJ]$
- U is the internal energy $[kJ]$
- $\dot{m}_l$ is the blowby flow $[kg/s]$
- h_l is the enthalpy of the blowby $[kJ/kg]$
- ω is the engine speed $[rad/s]$

However, the blowby flow is partially responsible for hydrocarbons emission and lower engine performance due to its involvement in quench effect. Its impact is, then, considered to be minimal for nitric oxide emissions. Therefore, for the rest of the methodology, the blowby flow is assumed to be equal to zero and thus negligible. This assumption is further discussed in Section 4.

2.2.1 Finite Energy Release

By developing (2.12) and considering that the gases involve in the engine cycle are ideal gases,

$$\begin{aligned} pV &= \nu R_u T \\ \delta W &= pdV \\ dU &= c_v dT \end{aligned}$$

the energy balance equation becomes,

$$\delta Q - pdV = \frac{c_v}{R}\left(p\frac{dV}{d\theta} + V\frac{dp}{d\theta}\right) \tag{2.13}$$

The equation for the pressure distribution and the heat distribution are then,

$$\frac{dp}{d\theta} = -\gamma\frac{p}{V}\frac{dV}{d\theta} + \frac{(\gamma-1)}{V}\frac{dQ}{d\theta} \tag{2.14}$$

$$\frac{dQ}{d\theta} = Q_{in}\frac{dx}{d\theta} - \frac{dQ_l}{d\theta} \tag{2.15}$$

Where γ, V, Q_{in}, x, Q_l are respectively the ideal gas coefficient, the working chamber volume, the heat released by the combustion, the burned mass fraction and the heat losses through the chamber walls. Thanks to the polytropic transformation, the mean gas temperature distribution is computed according to the pressure.

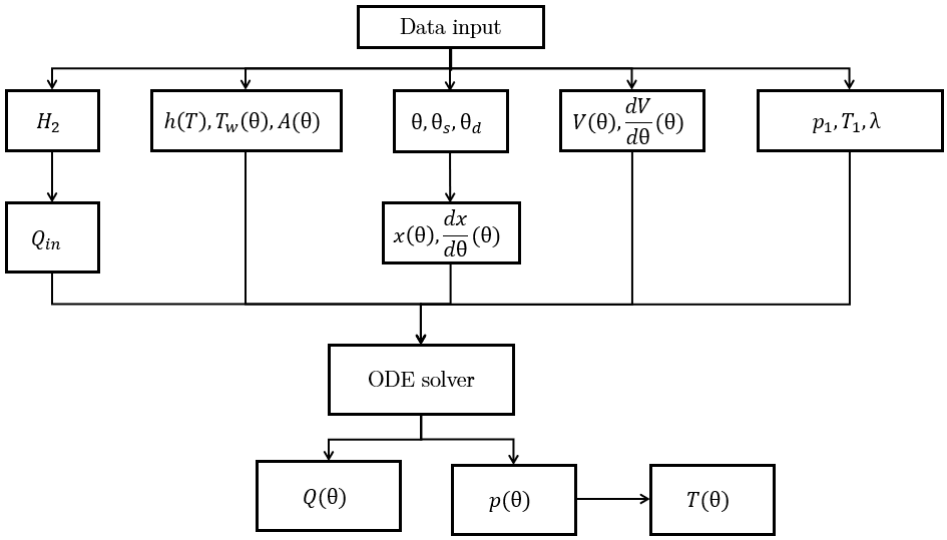

Figure 2.1: Finite Energy Release method

2.2.2 Homogeneous Two-Zone Finite Heat Release cycle

The Homogeneous Two-Zone Finite Heat Release (HTZ) cycle is an upgraded version of the FER model described in Section 2.2.1. It divides the combustion chamber into two zones to consider the evolution of the burned and unburned gases. This approach allows for a more accurate temperature distribution compared to the mean temperature computed by the original FER model.

Still based on the laws of conservation and the ideal gas assumption, this model also assumes that the two zones are at identical pressure and that the ignition temperature is the constant pressure adiabatic flame temperature introduced later in Section 2.6.

The goal is to compute the temperature evolution for the unburned (T_u) and the burned gases (T_b). By regrouping the computations of each parameter from (2.12) in Appendix A.2 and considering the properties of the burned and unburned gases,

the final system of equations becomes, [3]

$$\frac{dp}{d\theta} = \frac{A+B+C}{D+E} \tag{2.16}$$

$$\frac{dT_b}{d\theta} = \frac{-hA_c(T_b - T_w)}{\omega m c_{pb}\sqrt{x}} + \frac{T_b}{c_{pb}}\frac{\partial v_b}{\partial T_b}\frac{A+B+C}{D+E} + \frac{h_u - h_b}{x c_{pb}}\frac{dx}{d\theta} \tag{2.17}$$

$$\frac{dT_u}{d\theta} = \frac{-hA_c(1-x^2)(T_u - T_w)}{\omega m c_{pu}(1-x)} + \frac{T_u}{c_{pu}}\frac{\partial v_u}{\partial T_u}\frac{A+B+C}{D+E} \tag{2.18}$$

Where the coefficient A, B, C, D and E are,

$$A = \frac{1}{m}\frac{dV}{d\theta}$$

$$B = \frac{hA_c}{\omega m}\left[\frac{1}{c_{pb}}\frac{\partial v_b}{\partial T_b}\sqrt{x}(T_b - T_w) + \frac{1}{c_{pu}}\frac{\partial v_u}{\partial T_u}(1-\sqrt{x})(T_u - T_w)\right]$$

$$C = -(v_b - v_u)\frac{dx}{d\theta} - \frac{\partial v_b}{\partial T_b}\frac{h_u - h_b}{c_{pb}}\frac{dx}{d\theta}$$

$$D = x\left[\frac{T_b}{c_{pb}}\left(\frac{\partial v_b}{\partial T_b}\right)^2 + \frac{\partial v_b}{\partial p}\right]$$

$$E = (1-x)\left[\frac{T_u}{c_{pu}}\left(\frac{\partial v_u}{\partial T_u}\right)^2 + \frac{\partial v_u}{\partial p}\right]$$

Where :

- u and b are the suffixes for unburned and burned gases
- v is the specific volume $[m^3/kg]$
- c_p is the specific heat capacity at constant pressure $[J/kg/K]$
- x is the burned fraction rate
- h_i is the specific enthalpy $[J/kg]$
- h is the convective heat transfer coefficient $[W/m^2/K]$

2.3 Thermodynamic properties

In this section, two combustion equations are considered for the computations of the thermodynamic states of the burned and unburned gases, first, a more general equation and, second, the equilibrium concentration of the combustion products.

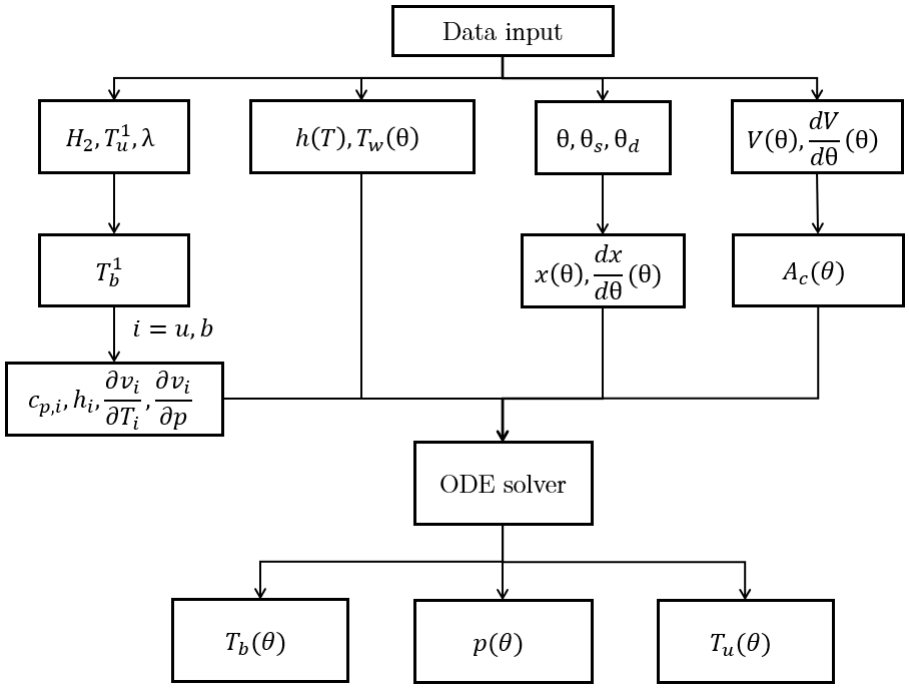

Figure 2.2: Homogeneous Two-Zones Heat Release method

2.3.1 General combustion equation

The oxidation of hydrogen is consider to respond to the reaction,

$$\nu_f H_2 + \nu_a(O_2 + 3.76N_2) \rightarrow \nu_0 H_2 + \nu_1 O_2 + \nu_2 H_2O + 3.76\nu_a N_2 \tag{2.19}$$

To identify the weighted reaction of (2.19), note that the presence of H_2 in the products is due to incomplete combustion with a lack of oxygen. Therefore, there is not enough oxygen to react with all the hydrogen.

Incomplete combustion can also occur due to *quenching*, where the combustion process stops prematurely because of heat exchanged with the combustion chamber wall. However, due to the complexity of modeling this phenomenon and its minor influence on NO formation, the quenching effect is neglected in this model.

After developing (2.19) for different fresh gas mixture cases, the following weighted reaction becomes,

$$H_2 + \frac{1}{2\phi}(O_2 + 3.76N_2) \rightarrow \frac{\phi - 1}{2\phi} H_2 + \frac{1 - \phi}{4\phi} O_2 + \frac{1 + \phi}{2\phi} H_2O + \frac{3.76}{2\phi} N_2 \tag{2.20}$$

where ϕ is the equivalence ratio, which defines the deviation of the air-fuel mixture from stoichiometric conditions. If $\phi = 1$, the mixture is said to be at *stoichiometric*

conditions where the only products resulting from the combustion are H_2O and N_2. However, ϕ has upper and lower bounds within which the mixture still ignite. If $\phi > 1$, the mixture is rich, resulting in incomplete combustion. If $\phi < 1$, the mixture is lean, with more oxygen than needed to react with all the fuel, resulting in the presence of O_2 in the products.

2.3.2 Chemical equilibrium

In high temperature conditions, the dissociation of molecules of the products resulting from (2.19) must be taken into account creating more species in the combustion process,

$$\begin{aligned} H_2 + \frac{1}{2\phi}(O_2 + 3.76N_2) \rightarrow & \nu_1 H_2 0 + \nu_2 N_2 + \nu_3 O_2 + \nu_4 H_2 \\ & + \nu_5 H + \nu_6 O + \nu_7 OH + \nu_8 NO \end{aligned} \tag{2.21}$$

The stoichiometric coefficients, ν_i, are computed by solving the system of equations resulting from the atom balance, the molar fraction sum, and the gas-phase equilibrium reactions,

$$\begin{aligned} \frac{1}{2}H_2 &\rightleftharpoons H \\ \frac{1}{2}O_2 &\rightleftharpoons O \\ \frac{1}{2}O_2 + \frac{1}{2}H_2 &\rightleftharpoons OH \\ \frac{1}{2}O_2 + \frac{1}{2}N_2 &\rightleftharpoons NO \\ H_2 + \frac{1}{2}O_2 &\rightleftharpoons H_2O \end{aligned}$$

Thus, eight equations are obtained for eight unknowns. By solving this system (see Appendix A.2), the stoichiometric coefficients of the combustion equation are computed. After identifying these coefficient, Olikara and Borman [16] proposed the following computation for the thermodynamic properties of the burned gases

using curve-fit data in Appendix B,

$$h = \sum_i h_{o,i} y_i \tag{2.22}$$

$$c_p = \sum_i \left(c_{po,i} + h_{o,i} T \frac{dy_i}{dt} \right) \tag{2.23}$$

$$\frac{\partial v}{\partial T} = \frac{v}{T} \left(1 - \frac{T}{M} \sum_i (M_i \frac{dy_i}{dT}) \right) \tag{2.24}$$

$$\frac{\partial v}{\partial p} = \frac{v}{p} \left(1 - \frac{p}{M} \sum_i (M_i \frac{dy_i}{dp}) \right) \tag{2.25}$$

Where :

- suffixes o is the thermodynamic property computed from the curve-fit data
- suffixes i corresponds to the combustion product
- M is the molecular weight $[kg/kmol]$
- h is the specific enthalpy $[J/kg]$
- c_p is the specific heat capacity at constant pressure $[J/kg/K]$

2.4 Working chamber

The combustion chamber volume of a rotary engine varies depending on the crank angle, θ, by tracing a *peritrochoid* curve. The volume of the working chamber is thus approximated by K. Yamamoto, [29].

$$\begin{aligned} V(\theta) &= bF(\theta) \\ &= b \left[\frac{\pi}{3} e^2 + eR \left(2\cos(\phi_m) - \frac{3\sqrt{3}}{2} \sin\left(\frac{2}{3}\theta + \frac{\pi}{2} \right) \right) \right] \\ &+ b \left[\phi_m \left(\frac{2}{9} R^2 + 4e^2 \right) \right] \end{aligned} \tag{2.26}$$

Where :

- e : the amount of eccentricity $[m]$
- b : the width of the rotor housing $[m]$
- R : the generating radius $[m]$
- ϕ_m : the maximum angle of oscillation $[deg]$

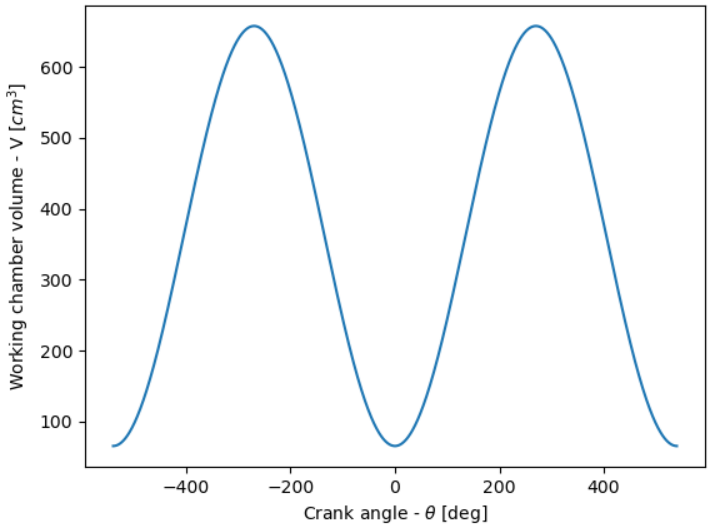

Figure 2.3

- $F(\theta)$: the side area of the working chamber $[m^2]$

The derivative of the working chamber volume become then,

$$\frac{\partial V}{\partial \theta} = -\sqrt{3}ebR\cos\left(\frac{2}{3}\theta + \frac{\pi}{2}\right) \tag{2.27}$$

The evolution of the volume in the combustion chamber is represented in Figure 2.3. From (2.26), the in-wall area of the working chamber can be determined. Considering the engine design in Figure 1.7, the working chamber is exposed to four areas:

1. The rotor's side
2. The housing
3. The side housing

The complex shape of the working chamber has been approximated by Danieli, Et al [8] which constitute a great approximation by comparison with Ansdale's calculations, [19]

$$\frac{A}{2} = \frac{V(\theta)}{b} + \frac{V(\theta)}{L} + bL + C \tag{2.28}$$

Where C corresponds to a correction factor taking into account the 10% error cause by the approximation.

2.5 Mass fraction burned

The concentration of fresh and burned gas vary as the combustion process occurs. Thus, the proportion of burn gases during the combustion is defined by the following,

$$x(\theta) = \frac{1}{2}\left[1 - \cos\left(\frac{\pi(\theta - \theta_s)}{\theta_d}\right)\right]$$

Where :

- θ_s is the crank angle where the combustion starts $[deg]$
- θ_d is the duration of the combustion $[deg]$

As the angle of combustion initiation is a parameter set in engine tuning and impacts the engine's performance, the combustion duration, however, is a complex parameter to identify theoretically. Indeed, it depends on many factors such as air-fuel richness, turbulent flame regime, fluid speed, etc. Therefore, θ_d is an experimental value obtained in laboratory settings, typically set to 70 degrees under lean mixture conditions [18][8].

Although considering θ_d as a constant, as shown in [10], it's important to note that its value also varies depending on the equivalence ratio, ϕ. The turbulent flame propagation speed, directly proportional to the laminar flame speed defined in (2.29), highly depends on the air-fuel mixture richness.

$$S_{L,H_2} = \sqrt{-\frac{2\alpha_{th}}{\rho_{in}}(m_F + m_a) < \dot{\omega}_F >} \tag{2.29}$$

Where :

- suffixes F and a corresponds to fuel and air respectively
- α_{th} is the thermal diffusivity $[m^2/s]$
- ρ_{in} is the density $[kg/m^3]$
- m is the mass $[kg]$
- $\dot{\omega_F}$ the rate of reaction $[mol/s]$

2.6 Adiabatic flame temperature

The flame temperature is the temperature of the products as they burn. During this process, no work from the shaft is involved, and as the flame is initially not in contact with any combustion chamber walls, the computation considers this

temperature in adiabatic conditions, denoted as T_{ad}. There are two ways to compute this temperature: considering constant pressure, $T_{ad,p}$, or constant volume, $T_{ad,v}$, depending on the type of engine used. As combustion in spark-ignition engines occurs at constant volume, it would be evident to use the constant volume adiabatic flame temperature definition. However, $T_{ad,v}$ is greater than $T_{ad,p}$, which has a value closer to real conditions. Therefore, it would be wiser to compute $T_{ad,p}$ for this application. By considering the adiabatic condition with the conservation of enthalpy,

$$H_r = H_p \tag{2.30}$$

Where r and p correspond to the reactants and the products of the combustion equation. By using the ideal gas approximation, (2.30) becomes,

$$H = H^f + H^s(T) = H^f + C_p(T)\Delta T$$

$$H_r^f + \int_{T_s}^{T_{in}} \sum_{i=R} C_{p,i}\, dT = H_p^f + \int_{T_s}^{T_f} \sum_{j=P} C_{p,j}\, dT$$

$$H_r^f + (T_{in} - T_s) \sum_{i=R} < C_{p,i} >_{T_s}^{T_{in}} = H_p^f + (T_f - T_s) \sum_{j=P} < C_{p,j} >_{T_s}^{T_f}$$

Where the *Lower Heating Value* is defined as the the amount of heat released from the combustion of a molecular species,

$$LHV = H_r^f - H_p^f$$

With a same resolution for the conservation of internal energy, the equation obtained for the constant pressure case is,

$$T_{ad,p} = T_s + \frac{LHV + (T_{in} - T_s) \sum_R < C_{p,i} >_{T_s}^{T_{in}}}{\sum_P < C_{p,j} >_{T_s}^{T_f}} \tag{2.31}$$

Considering (2.31), an iteration process is needed to compute the calorific capacity of the products. Therefore, Figure 2.4a illustrates the iteration process. First, the calorific capacity of the reactants is computed with an initial temperature set. Next, the lower heating value is evaluated by setting the reference temperature and the species involved in the combustion process. After that, a first guess for the flame temperature allows to compute the constant pressure heat capacity, c_p, of the products and, finally, the adiabatic flame temperature. However, if the variation between the estimated temperature before the iteration and the final computed one is higher than the iteration threshold, the iteration process continues until the condition is met. Figure 2.4c shows that only four iterations are needed to obtain a satisfactory result.

Figure 2.4b demonstrates the strong dependency of T_{ad} to the equivalence ratio in atmospheric conditions and shows a flame temperature of 2390 $[K]$ in stoichiometric conditions, $\lambda = \phi = 1$. However, in SI, the compression stroke operates before the combustion increases the temperature of the fresh gases, T_{in}, and thus the flame temperature.

2.7 Heat analysis

2.7.1 Combustion energy

$$Q_{in} = m_f q_c = m_f \left(\sum_{i=R} H_i - \sum_{j=P} H_j \right) \tag{2.32}$$

Where m_f is the fuel's mass and q_c, the heat of combustion.

2.7.2 Heat losses

The burned gases exchange heat with the chamber walls due to their temperature difference. Three heat transfer methods exist : convection, conduction and radiation. However, some of them are negligible because their contribution is very small and complex compared to the others. Therefore, heat transfer from radiation is negligible compare to convection and conduction transfer. Heat transfer from conduction is not consider because the study is restrained for the exchange between the combustion chamber and the in-housing wall.

The heat transfer between the combustion chamber and the inside wall of the housing is defined by Newton's law,

$$\dot{Q} = h_c A (T - T_w) \tag{2.33}$$

Where the in-housing surface A is computed in section 2.4. The temperature of the in-wall, T_w, and the convective heat transfer coefficient, h_c, are yet to be determined.

In-wall temperature distribution

The rotary engine does not operate its four strokes in the same volume like reciprocating engines. Therefore, by considering this property and the characteristic of longer exposure to the in-housing walls, assuming constant wall temperature in the steady-state conditions can not be applied. Figure 2.5a illustrates, for gasoline application, that the maximum temperature is located after the TDC position where the combustion process majorly occurs.

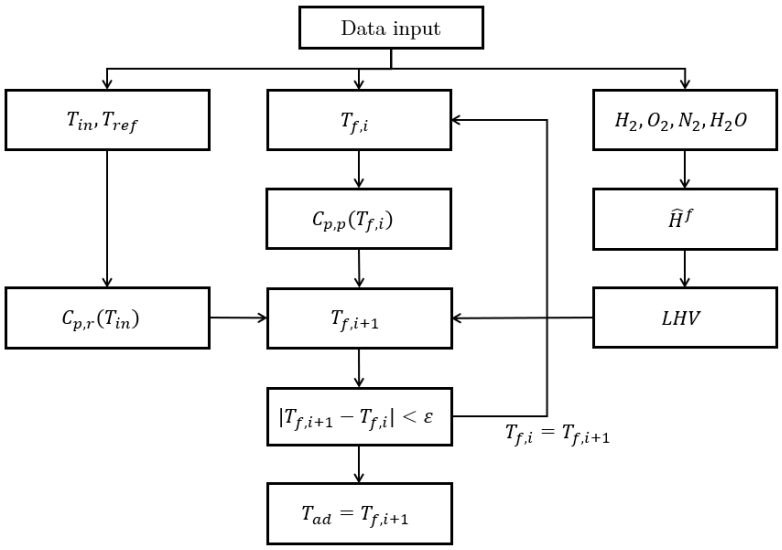

(a) Iteration process for the adiabatic constant pressure temperature

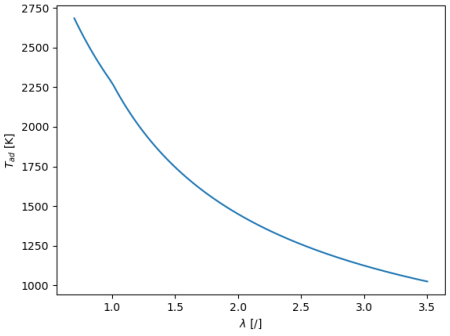

(b) Variation of T_{ad} at constant pressure according to λ

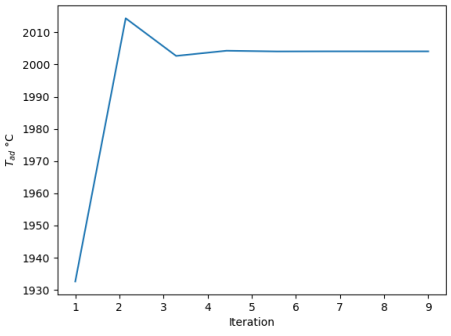

(c) Convergence to the final adiabatic flame temperature

Figure 2.4: Computation of T_{ad} with $T_{in} = 300\ [K]$

It could be interesting to precise that, in piston engines, the high temperature load is equal in every space of the in-cylinder wall. However, in this case, the side housing is less exposed than the rotor housing to high temperature loads due to the positioning of the spark. Therefore, the materials could differ between the side housing composed of cast iron and the rotor housing design with either gamma silmin aluminium alloy or cast iron. The material choice depends on the application of the engine, the cost efficiency but also the surface treatment needed to minimise the sealing wear.[29]

The precise temperature distribution is obtained experimentally. However, for the application, the temperatures obtained for gasoline application are used. This means that, in reality, the wall temperature could be greater. It is also interesting to underline that, after looking at the water cooling system in rotary engine (cfr. Appendix C.3) the water passes first nearby the TDC position. There, it increases its temperature by "absorbing" the heat released by the combustion. After, the water passes through the compression and expansion side of the housing where the gas temperature could be lower, thus, the water released some of its heat. This preheats the fresh gases eases the combustion of the mixture.

After considering the temperature distribution in Figure 2.5a, a regression provides the temperature distribution of the inner wall in function of the crank angle sensor at 4000 $[rpm]$,

$$\begin{aligned} T_w(\theta) = &- 5.45 \times 10^{-17}\theta^7 - 7.88 \times 10^{-15}\theta^6 + 3.09 \times 10^{-11}\theta^5 \\ &+ 4.58 \times 10^{-9}\theta^4 - 5.45 \times 10^{-6}\theta^3 - 7.81 \times 10^{-4}\theta^2 \\ &+ 0.32\ \theta + 4.27 \times 10^2 \end{aligned} \tag{2.34}$$

Convective heat transfer coefficient

Woschni developed an equation describing the convective heat transfer coefficient through an ICE cycle. This universal equation results from experimental analysis on a gasoline reciprocating engine, [28]

$$h_c = C d^{m-1} p^m w^m T^{0.75-1.62m} \tag{2.35}$$

Where :

- $C = 0.013$ for hydrogen powered engines [14]
- $m = 0.8$ considering turbulent fluid flow in pipe
- d is the characteristic length $[m]$

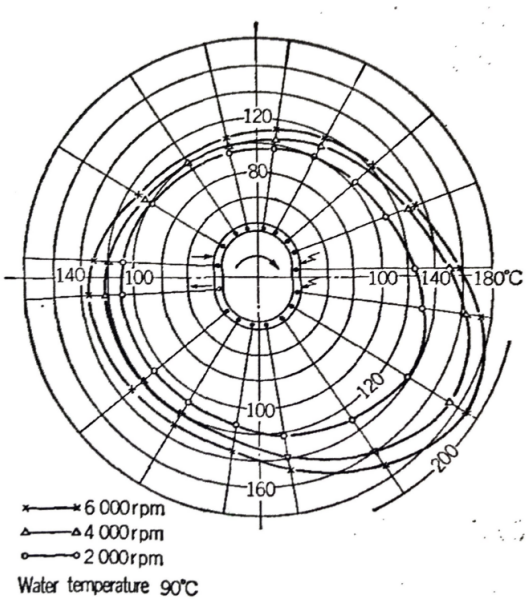

(a) Inner surface temperature of the housing with water at 90° [29]

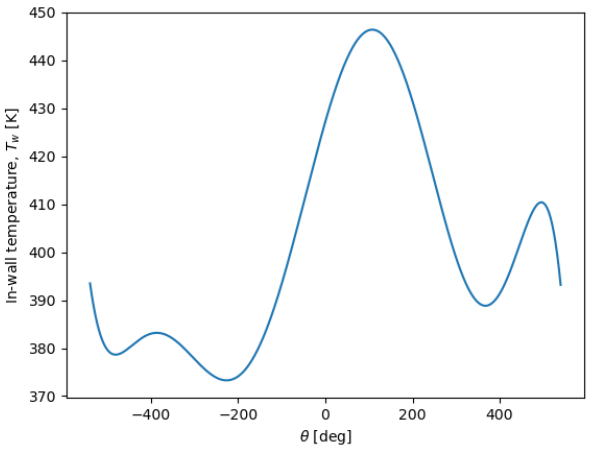

(b) Seventh order T_w regression at 4000 $[rpm]$

Figure 2.5: Computation of T_w

- p is the mean pressure $[Pa]$
- T is the mean temperature $[K]$
- w is the mean gas velocity $[m/s]$

Due to the complexity of identifying the mean gas velocity, Woschni wrote an expression based on the piston speed w_m and the speed of gas contribution during combustion, w_c,

$$w = C_1 w_m + w_c \tag{2.36}$$

It is important to note that the constant C_1 value differs depending on the stroke the engine is operating, 6.18 during scavenging strokes with no contribution from the combustion gas and 2.28 for compression and expansion strokes. Finally, w_c equals to,

$$w_c = C_2 \frac{V_s T_1}{p_1 V_1}(p - p_m) \tag{2.37}$$

Where C_2 is equal to 0.00324 $[m/s\ deg]$ and,

- V_s is the displacement $[m^3]$
- V_1 is the volume at start of the combustion $[m^3]$
- T_1 is the temperature $[K]$
- p_1 is the pressure $[Pa]$
- p_m is the motoring pressure $[Pa]$

Danieli, Et al developed for the rotary engine a definition for the rotor speed, w_m, and the characteristic length, d,[8]

$$w_m = \frac{r\omega}{3} \tag{2.38}$$

$$d = 2\left(\frac{1}{b} + \frac{bL}{V}\right)^{-1} \tag{2.39}$$

2.8 Residual factor

The residual factor allows to simulate the impact of gas mixtures from different sources. In reciprocating engines, the residual factor represents the mixing of exhaust and fresh gases during the overlap between the opening of the exhaust valve and the closing of the intake valve at the scavenging process.

For RE, the scavenging process has a minimal impact on the residual fraction because the overlap of the exhaust and intake ports is only about 3 to 5 degrees

and their is no scavenging process. However, the engine is well known for its leaks between combustion chambers. Danieli Et al. developed a formula to compute the *effective residual mass fraction* [8]:

$$f = \frac{m_r + m_{lb}}{m_{int} + m_r + m_{lb}} \tag{2.40}$$

where:

- m_r is the residual mass $[g]$
- m_{int} is the intake mass $[g]$
- m_{lb} is the mass leak with the other combustion chambers $[g]$

Using this equation, Danieli Et al. measured a residual fraction of 0.11 for low engine loads. However, this value could vary with hydrogen uses because of its diffusivity, but because of the absence of experimental research, this value is kept and a sensitivity work is done in Section 4 on NO prediction.

The equation (2.41) introduced in [3], where the residual factor is computed by comparing the concentration of a specific molecule from (2.3.1) to the actual measured value, would not be reliable in REs due to the uncertainty of the composition of the oil injected to lubricate the rotor.

$$f = \left[1 + \frac{m'}{m''}\left(\frac{y''_{CO_2}}{y_{CO_2}} - 1\right)\right] \tag{2.41}$$

Where :

- m' and m'' are the mass of the fuel-air mixture and residual respectively $[g]$
- y_{CO_2} is the quantity of carbon dioxide resulting from the combustion
- y''_{CO_2} is the quantity of residual carbon dioxide

2.9 Parameterization

This chapter lists the adaptations made for rotary engines. As each parameter has been modified, many factors are identifiable as important in engine tuning and design. These parameters are important because they form the basis of an emission analysis and simulation sensitivity in Section 4. These factors are the following :

Equivalence ratio, ϕ : characterises the proportion of fuel mixed with air deviated from the stoichiometric conditions. As explained in Section 2.3.1, this parameter indicates if the mixture is rich ($\phi > 1$) or lean ($\phi < 1$). It would

dictate the species present in the combustion products. This value can be also found in literature under its opposite definition, the excess-air coefficient ($\lambda = 1/\phi$).

Start of combustion, θ_s : governs the beginning of the combustion process. It impacts the burned fraction rate coefficient and is an important factor in engine tuning. Its value will advance ($\theta_s < 0°$) or delay ($\theta_s > 0°$) the combustion in the cycle, causing it to start either at the end of the compression phase or at the beginning of the expansion phase. Its impact is well known for engine performance, but its consequences for emissions analysis are more complex.

Engine speed, Ω : indicates the amount of time the gas in the working chamber is exposed to the chamber walls. Thus, its impact is primarily on the heat exchange process.

Initial states: are necessary for the computation to start the integration process of the HTZ cycle. Initial pressure and temperature can vary either due to atmospheric conditions (altitude) or due to forced induction devices (turbocharger, supercharger, ...). Increasing or decreasing these values will change the curve of pressure and temperature inside the engine cycle, thereby impacting NO.

Heat exchange : is primarily governed by Woshni's coefficient, h_c, and its identification is complex. Therefore, it is important to analyse the sensitivity of the simulation with respect to h_c.

Residual fraction, f : has not yet been defined in hydrogen application in RE. Even though this model uses the highest value measured for gasoline to compensate for the high diffusivity of hydrogen, this model could be sensitive to this value. Proper analysis should be conduct to understand its impact.

Chapter 3

Experimental methodology

This chapter elucidates the procedure established for measuring the exhaust gas composition from a rotary engine. It begins with a presentation of the engine utilized in the experimentation. Subsequently, it delves into the chosen method for hydrogen supply, followed by the methodology employed to identify the concentration of nitric oxide in the emissions. Finally, it outlines the experimental measures necessary for results analysis.

3.1 Engine specifications

The bench is equipped with a *Mazda 13B-T* engine. Dating from 1989, it previously powered a *Mazda FC3S S5 Turbo RX-7 Turbo-II*. Appendix C compiles all the work done on the engine to adapt it to the bench test and to both gasoline and hydrogen fuel use.

To provide some background on this engine, the *13* denotes a total displacement of 1.3 $[l]$ between the two rotors, and B signifies the second generation of rotary engine produced by Mazda, succeeding the $12A$. The designation $Turbo - II$ refers to the twin-scroll turbocharger, where the inlet turbine housing is divided, and the exhaust manifold design pairs the correct cylinders to direct flow into each scroll independently [21]. Table 3.1 regroups the specification.

3.2 Bench operation

The engine is modified to work under gasoline and hydrogen. The point is to progressively transit from gasoline to hydrogen while the engine is operating.

Specification	Value
Displacement [L]	0.654×2
Eccentricity [mm]	15
Generating Radius [mm]	105
Width [mm]	80
Compression ratio	9.0
Intake Charge Type	Turbocharged
Intake Type	Side Ported
Exhaust Type	Side Ported
Intake Open [ATDC]	3 °EA
Intake Close [ABDC]	65 °EA
Exhaust Open [BBDC]	50 °EA
Exhaust Close [BTDC]	3 °EA
Power	147 $[kW]$ (@6500 $[RPM]$)
Torque	360 $[Nm]$ (@3500 $[RPM]$)
Coolant	Water
Management	Drive-by-wire
ECU	Motec M130 GPR Rotary package

Table 3.1: Mazda 13B-T specification

To summarise the construction of the bench explained in Appendix C, the engine has been modified for research purpose. Therefore, the front grilles are replaced with two heat exchangers to cool down the water and the lubricating oil. The engine is fed in gasoline with the original fuel system and the fuel injectors are controlled by the ECU. The injection of hydrogen is, however, manually controlled by a flow meter valve system. Indeed, the hydrogen is continuously injected at constant flow in the air intake conduct before the separation in each rotor intake duct. This is to simplify the feeding system and ensure a homogeneous mixture.

3.3 Measurement setup

The composition of exhaust gases is measured using a *TESTO gas analyzer*, which is capable of quantifying the amount of NOx gases. Considering that nitric oxide is the primary precursor for the formation of nearly all nitrogen oxide gases, its concentration can be computed accordingly. The TESTO measures the concentration of nitrogen gases in parts per million (ppm).

3.4 Laboratory procedure

The objective of the experimental methodology is to determine if, in real life, the influence of the parameters involve in the variation of NO emissions aligns with the numerical model. Thus, the experimental work aims to measure the concentration variation according to various parameters. In this case study, the main focus is directed towards:

1. The equivalence ratio, ϕ
2. The engine speed, Ω
3. The start angle of combustion, θ_s

Therefore, the following tables should be completed,

Engine speed $= [RPM]$							
θ_s	-40	-35	-30	-25	-20	-15	-10
$\lambda = 1$							
$\lambda = 1.2$							
$\lambda = 1.8$							
$\lambda = 2$							
$\lambda = 2.5$							
$\lambda = 3$							
$\lambda = 3.5$							

Table 3.2: Second experiment table

This table enables to construct the λ-c_{NO}, the $RPM - c_{NO}$, and finally the $\theta_s - c_{NO}$ graphs.

To streamline measurement processes is to complete several tables according to the engine speed by filling Table 3.2. Initially, the engine speed is adjusted using the throttle opening potentiometer on the control panel on Figure 3.1. While adjusting the engine speed, the lambda value must be manually controlled. Since the ECU does not regulate hydrogen injection and the lambda sensor used is not adapted for hydrogen combustion, increasing the engine speed increases the quantity of air in the manifold, necessitating manual adjustment of hydrogen supply. Once the engine speed is set, the hydrogen injection flow is adjusted to achieve the desired equivalence ratio. Subsequently, the start of combustion is adjusted using the ECU's main ignition map. After measuring all values for different θ_s, the next λ value is set. Following the evaluation of concentrations for one speed at every combustion start angle for all equivalence ratios, the next speed is set, and so forth.

Figure 3.1: Control panel

Chapter 4

Results

This chapter interprets the results from the numerical simulation in order to better understand to emissions behaviours of the rotary engine while using hydrogen fuel. First, an examination of the different results obtained depending on the different methodologies proposed. Then, focusing on the most relevant one, this chapter analyses the impact of several parameters to consider in engine tuning. Finally, this section enunciate different ways to improve the numerical simulations.

4.1 Analysis

4.1.1 Model verification

Three computations where made to predict the states evolution and the nitric oxide formation. These methods differs on the computations of the thermodynamic states of the burned and unburned gases. The first one (HTZ1) computes the thermodynamics states at every temperature according to (2.19). the second one (HTZ2) computes the properties according to Olikara and Borman's numerical model introduced in Section 2.3.2 adapted from gasoline to hydrogen fuels. The last one (HTZ3) computes the thermodynamic states with (2.19) but uses the Wiebe burned fraction rate formula developed further in this chapter. [16]

Pressure evolution

To compare the reliability of the numerical methodology, only pressure measurements from [10] can be used as reference. Therefore, Figure 4.1 illustrates the differences between the experimental data and the model results. As the compression and the end of the expansion stroke are close to data, it as been observed

that there is a significant pressure difference during the combustion phase. This difference is explained by the use of (2.5) as burned fraction rate and not the formula developed by the Russian engineer, Ivan Wiebe,

$$x_b(\theta) = 1 - \exp\left[-a\left(\frac{\theta - \theta_s}{\theta_d}\right)^n\right] \tag{4.1}$$

This formula uses two factors : the *Wiebe efficiency*, a, and the *Wiebe form*, n. These two parameters are obtain empirically and depends on various conditions. Indeed, the efficiency factor can vary arbitrary from one to seven depending on the percentage of completion of the combustion process and the form factor depends on many factors as the combustion duration (engine design, load, speed, ...).

ϕ	θ_s $[^\circ BTDC]$	θ_d $[^\circ BTDC]$	a	n	**HTZ1** $[ppm]$	**HTZ3** $[ppm]$
$0,714$	3.6	68.5	4.12	1.05	95.04	1050
0.625	3.8	70.1	4.38	1.07	97.96	140.63
0.556	4	75.5	4.12	1.1	9.7	14.86
0.5	4.2	82	3.5	1.2	1.02	1.08

Table 4.1: Table of comparison from pressure data [10]

As Figure 4.2 illustrates the differences by using (4.1) instead of (2.5), Table 4.1 demonstrates the importance of the Wiebe burned fraction rate formula in predicting NO for different equivalence ratios at identical speeds. Figure 4.3 demonstrates the sensitivity of varying the value of the efficiency factor. Choosing the right value for the efficiency factor impacts the pressure curve, which explains the differences in nitric oxide emissions shown in Table 4.1. Even a unit difference can produce an almost five-bar pressure difference.

Temperature evolution

Figure 4.4 illustrates the differences of temperature between HTZ1, HTZ2 and HTZ3 for the 0.714 equivalence ratio conditions illustrate in Table 4.1. The first observation to make is the excessive temperature resulting from HTZ2 where HTZ1 and HTZ3 have a more realistic curve a direct consequence of the differences in the thermodynamic properties computation methodology. Also, there is a first net drop of temperature when the combustion starts. This phenomena is due to the fact that this model computes the adiabatic flame temperature according to the combustion equation (2.19). Further, the influence of Wiebe's formula shows as expected a steeper and higher temperature curve than HTZ1 meaning that the use of Wiebe's formula has, therefore, an non-negligible impact on temperature.

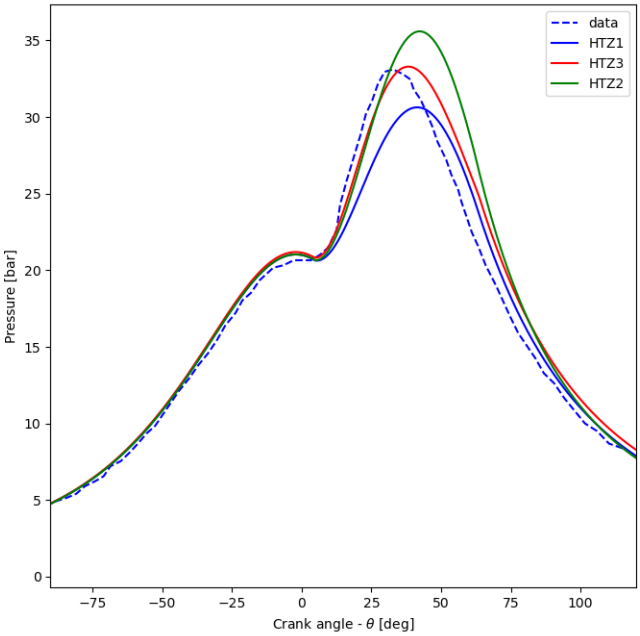

Figure 4.1: Pressure evolution for the HTZ1 model (blue) and HTZ2 model (green), HTZ3 (red) and experimental values (dotted) [10]

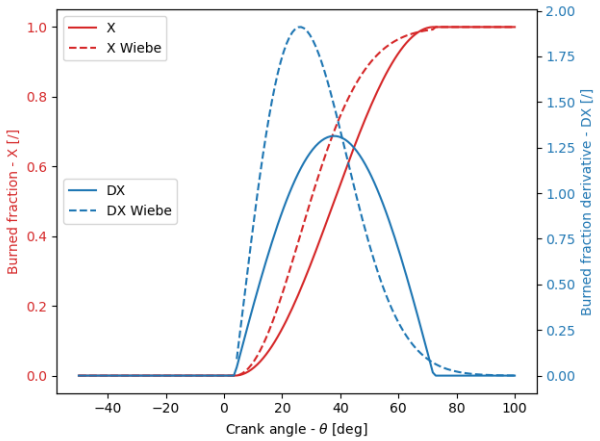

Figure 4.2: Burned fraction equation comparison

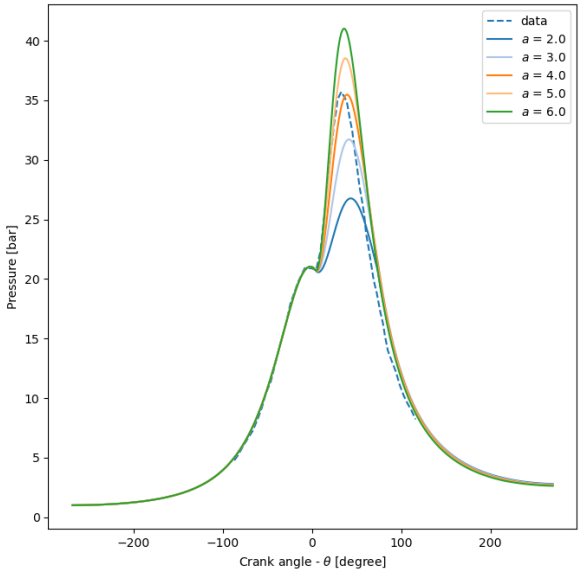

Figure 4.3: Sensitivity of the efficiency factor on the pressure curve

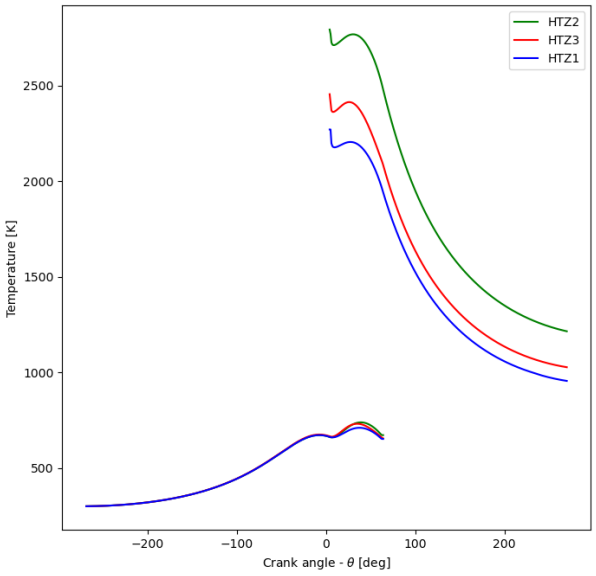

Figure 4.4: Temperature evolution of HTZ1 (blue), HTZ2 (green) and HTZ3 (red) model

Nitric oxide emissions

Finally, Figure 4.5 illustrates the difference of nitric oxide emissions computed from the three methods. As expected from the higher pressure and temperature curves, HTZ2 predict a dramatic amount of NO which is not correct according to the sources. However, HTZ1 and HTZ3 have a realistic value considering that it should obtain less NO than reciprocating engine (9000 $[ppm]$ measured) and that the peak of emissions is close to an equivalence ratio equal to 0.95. In addition, the use of Wiebe's formula predicts more nitric oxides due to the steeper pressure and temperature curves.

Therefore, it concludes that the Olikara and Borman model to predict the thermodynamic states of the burned gases resulting from the equilibrium equation in Section 2.3.2 is not suited for hydrogen fuel uses. Also the impact of Wiebe's burned fraction formula show a non negligible result compared to HTZ1. Therefore, for the rest of the study, the HTZ3 model will be the reference model. However, it is important to note that the factor a and n in (4.1) varies constantly and that there is a lack of experimental data to adapt this definition to all the engine conditions that it goes through. This could lead to a slight over-estimation or under-estimation to the exact emissions that the prediction model should return. Figure 4.5 shows the high sensibility of nitric oxide formation to temperature as expected from the literature.

4.1.2 Equivalence ratio

Figure 4.6 illustrates the impact of the equivalence ratio on the nitric oxide formation. There is a peak of emissions close to $\phi = 0.95$. The influence of ϕ is to be observed on the pressure and the temperature curves. As known, more it approach stoichiometric conditions less there is oxygen in the products to react with, but by looking at Figure4.7 and Figure 4.8, this explains the NO formation for the two different types of mixture.

In lean mixture, the concentration of oxygen in the products is rising enabling to create more nitric oxide. However, as shown in Figure 4.8, as ϕ approaches the flammability sub-limit, the temperature curves drop non-linearly. The temperature drops quickly below the temperature threshold of nitric oxide formation. Even though there is potential for more nitric oxide to form, the temperature conditions are not ideal to enable maximum NO formation.

In rich mixture, this model predicts small concentrations of nitric oxide. This is because in rich conditions the only reason why oxygen is accessible to react with nitrogen is because of the high temperatures that dissociates molecules liberating oxygen radicals enabling them to react with nitrogen. As the equivalence ratio

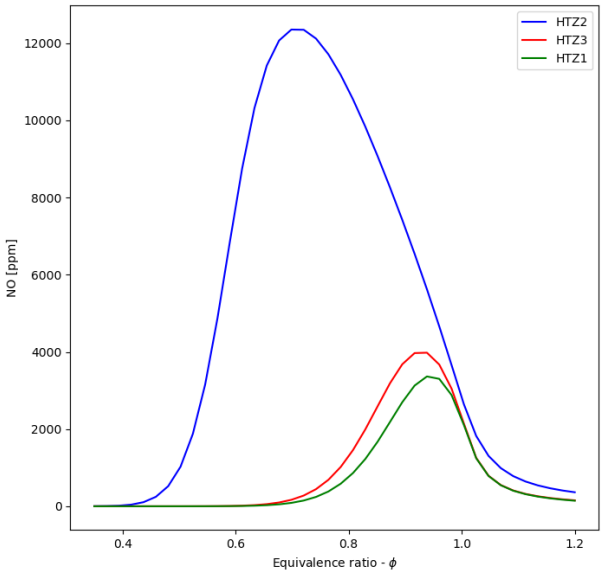

Figure 4.5: Concentration evolution using HTZ1 (red), HTZ2 (blue) and HTZ1 using Wiebe's formula (green)

increases, Figure 4.9 shows that the temperature drops not in the same rate than in lean mixture but enough to limit the dissociation of molecule and thus nitric oxide formation.

4.1.3 Engine speed

The engine speed influences on the time available for burned gases to exchange heat with the inside housing. Increasing the speed reduces then the impact of the in-wall contribution.

Figure 4.12 shows that NO increases as the engine speed increases. As the nitric oxide attain a peak at low engine speed for gasoline application [3], this peak is not reached by the engine before its speed limit. This is mainly due to the lack of heat losses capable to cool down the burned gas as shown in Figure 4.11. Even though there is no peak of emission, the emission profile in Figure 4.12 is increasing asymptotically proving that, at high speed, the emission concentration rate is decreasing as it reaches the maximal capacity of heat exchange. Indeed, the temperature profiles is dropping of at the beginning of the combustion because the heat exchanged is getting smaller assuming that, close to 10000 $[RPM]$, the

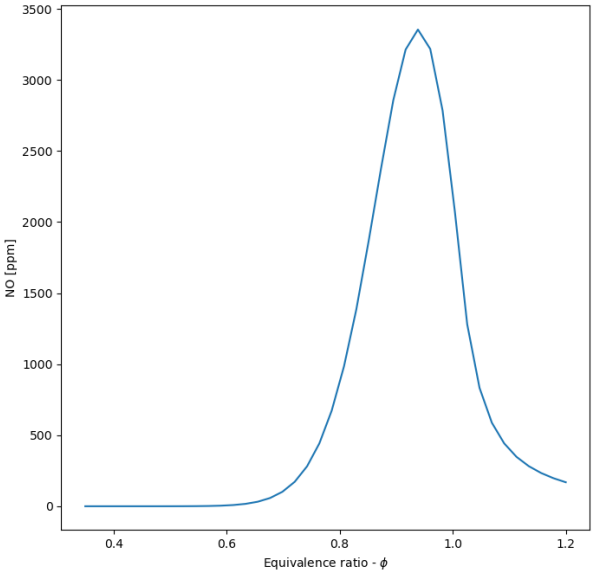

Figure 4.6: Nitric oxide formation

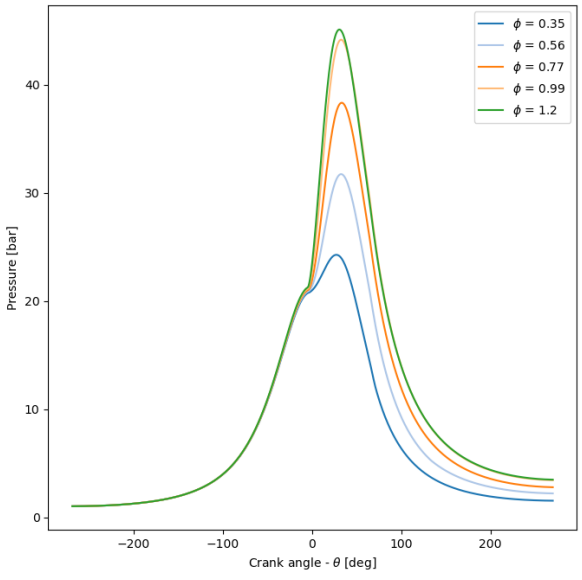

Figure 4.7: Pressure variation during a full engine cycle

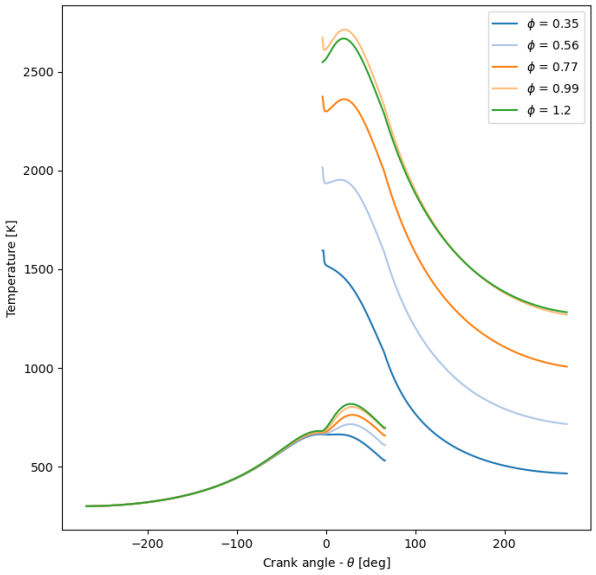

Figure 4.8: Temperature variation during a full engine cycle

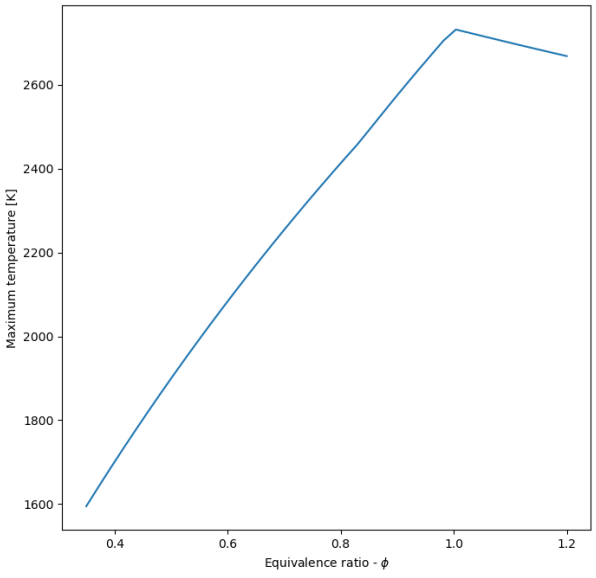

Figure 4.9: Maximum temperature in combustion chamber

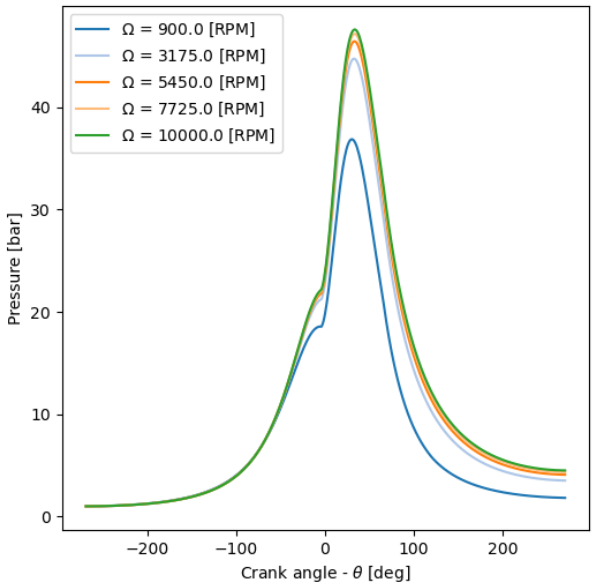

Figure 4.10: Pressure profile according to engine speed

system is approaching what it could be considered as adiabatic conditions.

4.1.4 Combustion start

Figure 4.15 illustrates the variation of nitric oxide emissions depending on the combustion start angle before the top dead center position for three equivalence ratios and engine speed values. Firstly, the impact of the combustion angle is very small close to the flammability limits. Approaching the peak of emissions, $\phi = 0.95$, the influence of the combustion start is non-negligible. As the ignition start is delayed, the concentration of nitric oxide decreases. This is primarily because delaying the ignition start significantly impacts the pressure profile. The peak pressure decreases substantially, as shown in Figure 4.13. Additionally, Figure 4.14 illustrates the impact of the combustion start angle on the temperature. Since pressure influences temperature, this decrease is explained because the peak temperature is delayed in the engine cycle. However, the lower sensitivity of the temperature curve compared to the pressure could because it is more sensible to the thermodynamic properties of the gas then the pressure. The thermodynamic properties depends primarily on the equivalence ratio and the temperature. Therefore, the sensitivity of the gas properties are lower for combustion starts variation then for equivalence ratio variation.

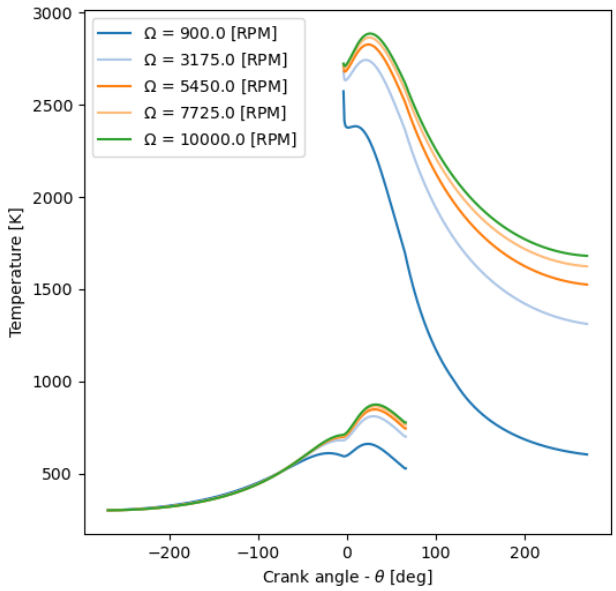

Figure 4.11: Temperature profile according to engine speed

4.1.5 Engine boost

This simulation uses initial conditions of pressure and temperature at the start of the compression stroke to compute the states of the gases through the mechanical strokes. In real life, engines are exposed to loads (for example, wheel friction). When the load is increasing, the engine sucks more fresh gases to compensate the resistance on the output shaft. More the inlet manifold pressure increases, more there is oxygen to react and thus more there is NO emitted as shown in Figure 4.16. However, this increases the indicated mean effective pressure (IMEP) too as shown in Figure 4.17 and thus increases the performance and the efficiency of the engine.

Figure 4.18 illustrates the benefits of engine boost. From an emission point of view, it shows that for identical engine setup but at higher intake pressure, the engine also delivers identical power for lower equivalence ratio and thus lower emissions. This is the main emission characteristic of engine boosting. However, increasing the initial temperature should better be as low as possible to reduce the fresh gas temperature at the initiation of the combustion. Downsizing the initial temperature will decrease the temperature curve and thus reduce NO as proven in Figure 4.19. This explains why engines emit less NOx in winter season and why there is an intercooler after engine boosters to reduce the increase of fresh gases temperature

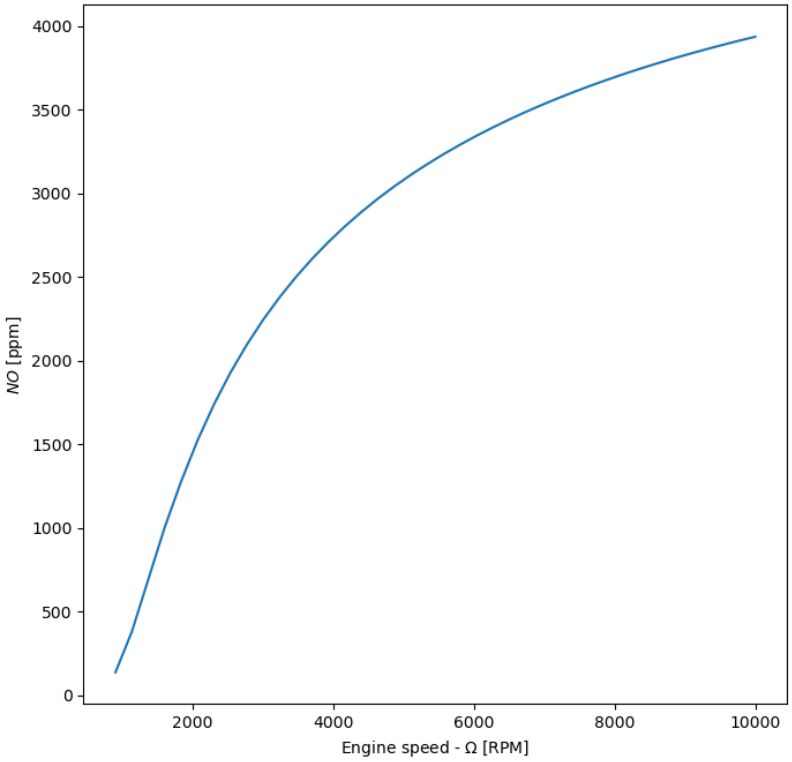

Figure 4.12: NO concentration according to engine speed at $\phi = 1$

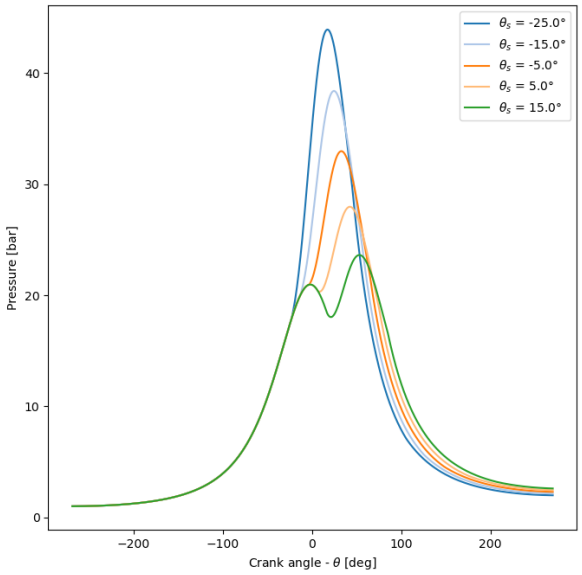

Figure 4.13: Influence of θ_s on the pressure profile

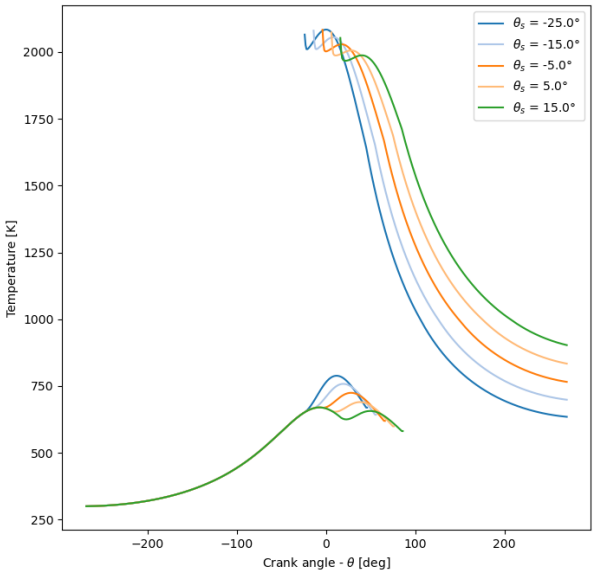

Figure 4.14: Influence of θ_s on the burned gas temperature profile

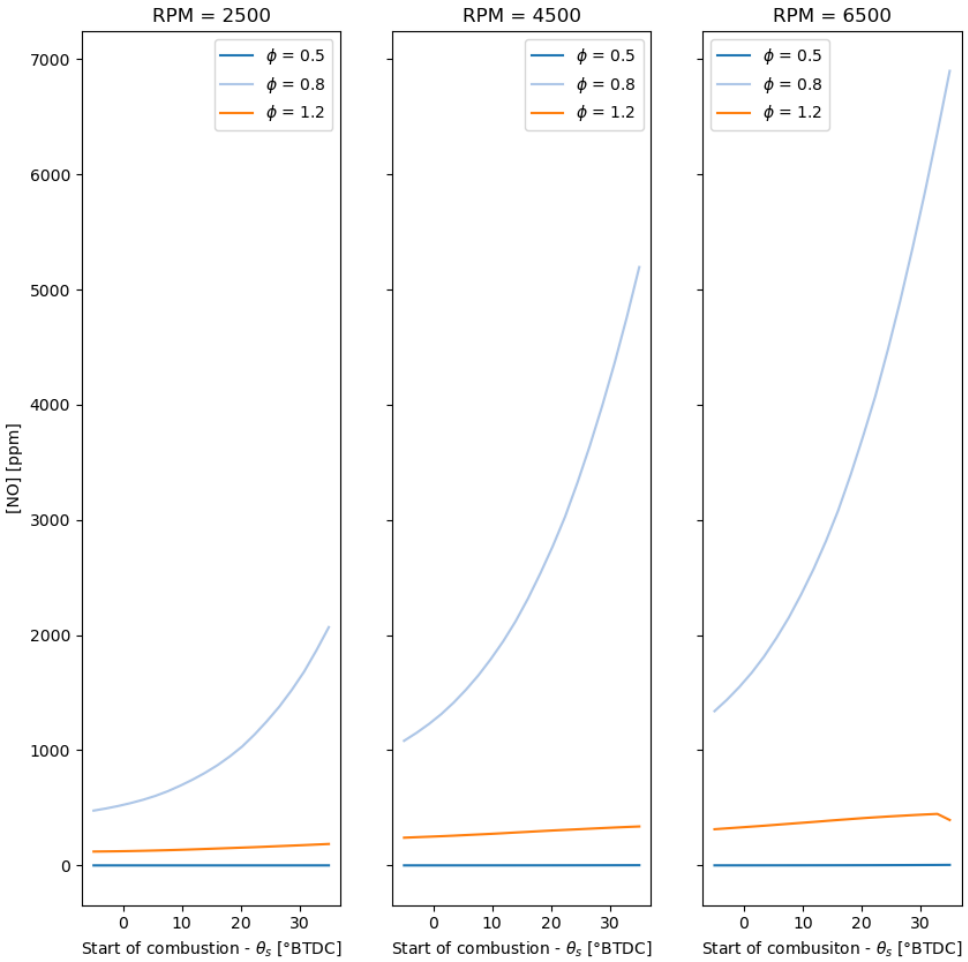

Figure 4.15: Variation of NO concentration according to the heat release start angle for different equivalence ratios and engine speeds

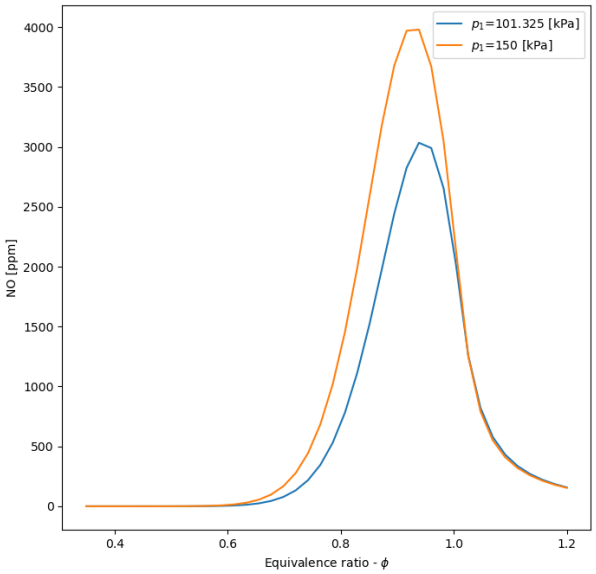

Figure 4.16: NO emission versus equivalence ratio

after compression.

4.1.6 Convective heat coefficient

As a parameter only part of simulation accuracy, it is interesting to explore the impact of the convective heat coefficient on the engine cycle. This is mainly to explain the complexity of modelling this parameter has many researchers are not agreeing on the formula to based their computation. Figure 4.20 illustrates the convection heat transfer coefficient computed according the Woschni's equation and the mean states of the combustion chamber calculated with the FER model introduced in Section 2.2.1. As this curve concur to Woshni's obtained values [28], many other sources predicts other values varying to sometimes almost twice the peak values.

Figure 4.21 illustrates the significant impact between different values for h_c equal to 0 to represent no heat losses, equal to 500 as constant value (often used in reciprocating simulations [3]) and equal to Woshni's equation. The consequences on the temperature curve have thus a significant impact on the prediction of nitric oxide as illustrated in Figure 4.22.

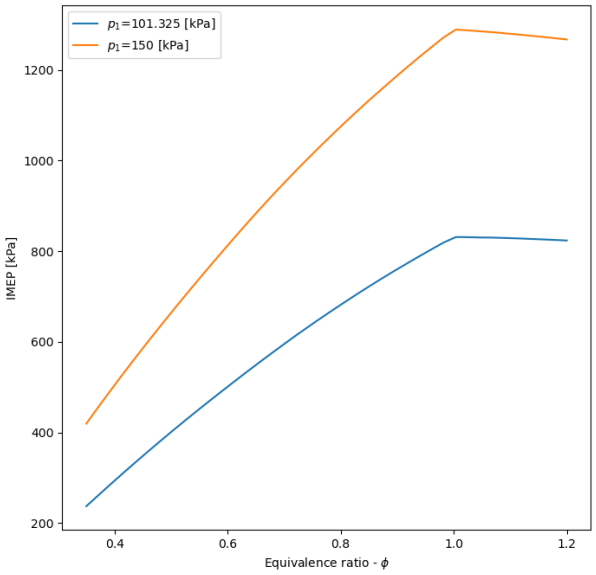

Figure 4.17: Indicated mean effective pressure versus equivalence ratio

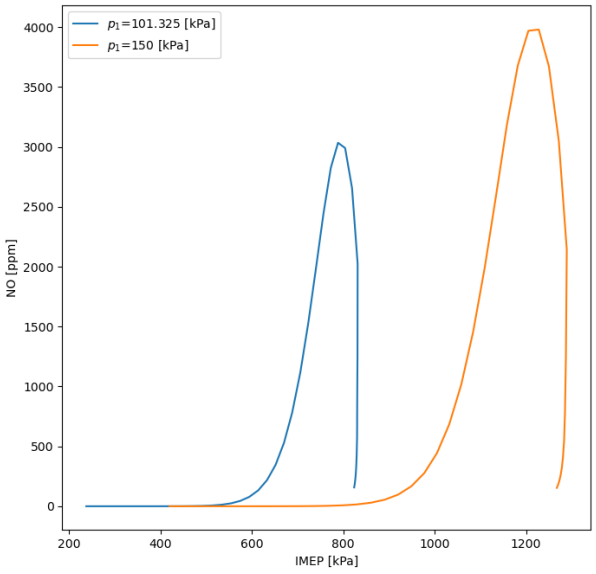

Figure 4.18: NO emissions versus Indicated mean effective pressure

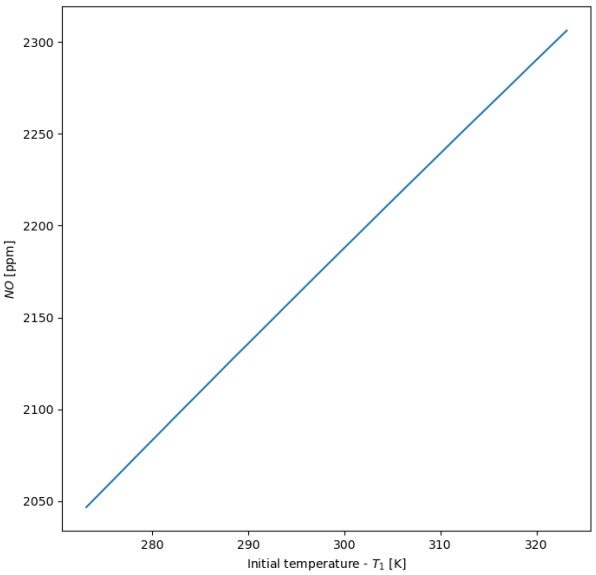

Figure 4.19: NO versus initial temperature

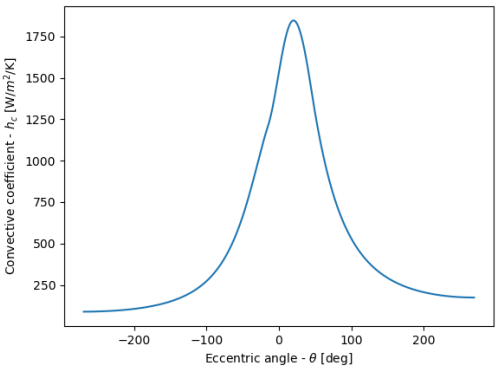

Figure 4.20: Woshni's coefficient through the mechanical strokes

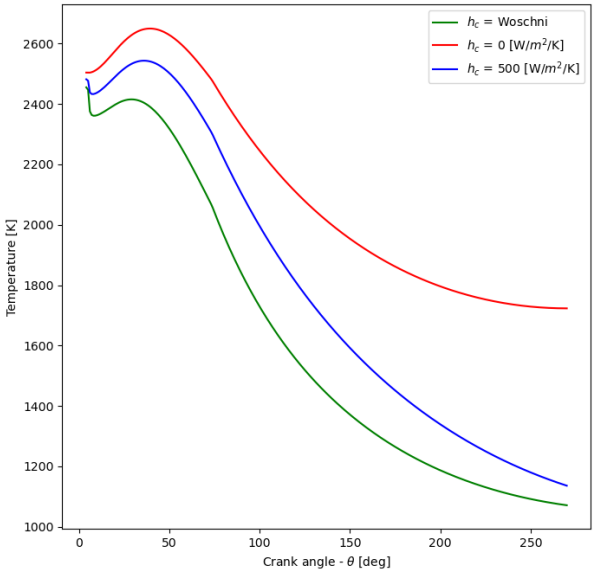

Figure 4.21: Influence of h_c on the temperature profile

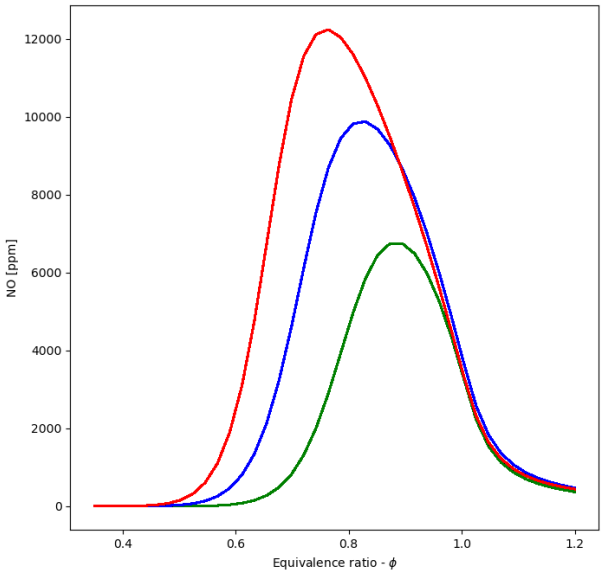

Figure 4.22: Influence of h_c on NO concentration for h_c equal to 0 (red), 500 (blue) and Woshni's formula (green)

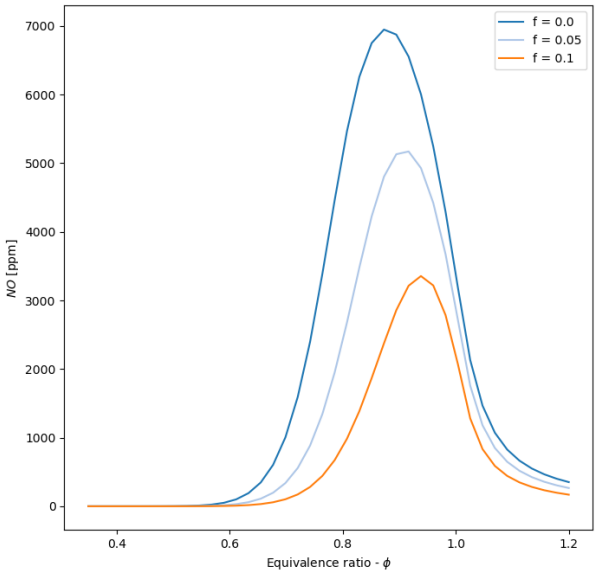

Figure 4.23: impact of residual fraction, f

4.1.7 Residual fraction

As last parameter to analyse, the residual fraction was considered in Section 2.8 equal to 0.1 according to Ferguson's, Et al work [8]. However, as said before, this value is meant to vary with the high diffusivity of hydrogen. Figure 4.23 demonstrates the high sensitivity of the residual fraction in the simulation reducing by almost 30 percent the amount of NO for a 5 percent increase in the residual fraction value.

4.2 Discussion

Even though this model enables to understand the behaviour of the engine's emissions using hydrogen as fuel, it is possible that the quantity of nitric oxide predicted overestimates the actual value that could be measured in the laboratory. For many reasons this nitric oxide simulation program could be improved.

First, some factors are not considered in this model because of lack of information and the necessity of complex experimental setup to identify them. These factors could affect the quantity of NO gases rejected in the exhaust pipes.

Second, observations in previous section shows that heat flux are a major parameter

to consider in the modeling and a precise model could be developed thanks to measurements.

Third, this study shows that starting the model with laboratory measurements, such as pressure curves, would improve the prediction model.

Finally, other existing model could even more precisely compute the engine states and thus the emissions such as multi-zone modeling. However, this kind of simulation program also has not yet been used for hydrogen rotary engines and could be a subject for further study.

4.2.1 Blowby coefficient

During the engine cycle, the gases are contained in the chamber thanks to the sealings. However, in reality, there are some leakage where the air exit the combustion chamber and is lost. These leakages can have a great impact on the engine's performance and emissions. Indeed these losses decrease the amount of oxygen in the combustion chamber impacting then the pollutants emissions. This is because the flame propagates into very narrow space, their quench effect causes the flame front to extinguish causing a premature stop of the combustion process and the presence of unburned fuel or hydrocarbons.[3]

Applying this phenomenon to the HTZ cycle helps to identify the importance of this coefficient and the close thermodynamic cycle assumption made for (2.12).

This blowby effect considers the engine's thermodynamic cycle to be open. This means that the cycle exchanges mass with its environment. Therefore, the energy balance equation become,[3]

$$\frac{dQ}{d\theta} - \frac{dW}{d\theta} = \frac{dU}{d\theta} + \frac{\dot{m}_l h_l}{\omega} \tag{4.2}$$

Where :

1. $\dot{m}_l$ is the blowby flow $[kg/s]$
2. h_l the enthalpy of the blowby $[J/kg]$

By introducing the definition of the blowby coefficient,

$$C = \frac{\dot{m}_l}{m} \tag{4.3}$$

The value of C is obtained experimentally because the blowby flow is computed by measuring the difference of pressure of compressible flow through an orifice. If

such expression exists for reciprocating engines, no experiments as been made for rotary engines. The blowby flow is defined as,[6]

$$\dot{m}_l = f(C, \frac{p_1}{p_2}, L) \tag{4.4}$$

Where,

1. p_1 and p_2 is the pressure in the chamber and in the cavity respectively
2. L is the sealing length

Figure 4.24 shows the minor influence of the blowby on nitric oxide emission. This is explained by the major impact of blowby in quench effect which is not involve in NO formation as detailed in Section 1.4.3. This conclude that the assumption considering a close thermodynamic engine cycle for NO emissions prediction is acceptable.

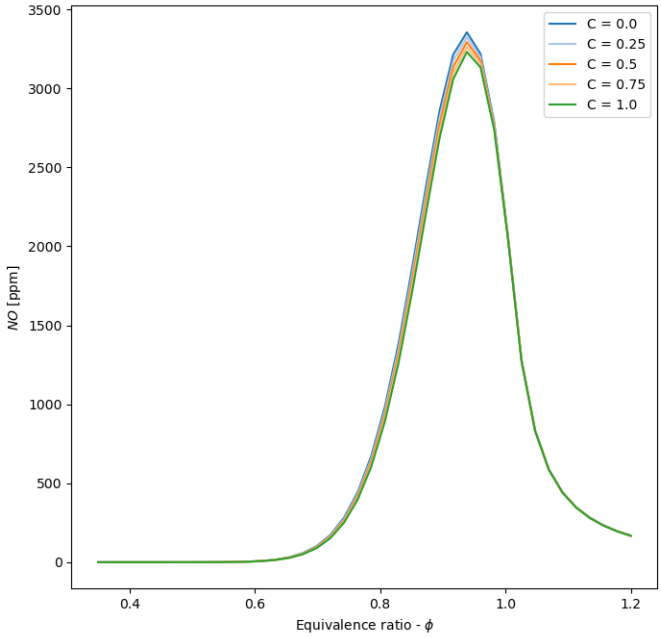

Figure 4.24: Influence of the blowby coefficient

4.2.2 Multi-zone model

After considering different nitric oxide gas emission predictions developed by others scientist, E.H. James concluded that to make the prediction of NO more accurate,

a multizone formulation should be considered to better represent the temperature gradient inside the burned gas zone. Therefore, he developed the first multizone model that will be improve later by Raine. [3][13]

The multizone shows that the two zone model from Ferguson overestimates the quantity of NO_x produced inside the combustion chamber and in fact the multizone model decreases the NO_x by 12% considering the heat transfers being uniform inside each separate zone. This prediction reaches its best approximation around ten zones but it also has limits such as fresh gases humidity (like the HTZ cycle) and influence of spark ignition advancement.[13]

This model consider multiple burned gas zones,

$$\frac{dp}{d\theta} = \frac{A + B_u + \sum(B_i) + \sum(C_i)}{\sum(D_i) + E} \tag{4.5}$$

$$\frac{dT_{bi}}{d\theta} = \frac{-hA_c(T_{bi} - T_w)}{\omega m c_{pbi}\sqrt{x}} + \frac{v_{bi}}{c_{pbi}}\frac{\partial \ln v_{bi}}{\partial \ln T_{bi}}\frac{dp}{d\theta} + \frac{h_u - h_{bi}}{x_{bi}c_{pbi}}\frac{dx_{bi}}{d\theta} - \frac{C(h_u - h_{bi}(1-x)}{\omega c_{pbi}} \tag{4.6}$$

$$\frac{dT_u}{d\theta} = \frac{-hA_c(1-\sqrt{x})(T_u - T_w)}{\omega m c_{pu}(1-x)} + \frac{v_u}{c_{pu}}\frac{\partial \ln v_u}{\partial \ln T_u}\frac{dp}{d\theta} \tag{4.7}$$

Where the coefficient A, B_u, B_i, C_i, D_i and E are,

$$A = \frac{1}{m}\left(\frac{dV}{d\theta} + \frac{VC}{\omega}\right)$$

$$B_i = \frac{h_{ci}A_c}{\omega m}\left[\frac{v_{bi}}{c_{pbi}}\frac{\partial \ln v_{bi}}{\partial \ln T_{bi}}\frac{x_{bi}(T_{bi} - T_w)}{\sqrt{x}T_{bi}}\right]$$

$$B_u = \frac{h_c A_c}{\omega m}\left[\frac{v_u}{c_{pu}}\frac{\partial \ln v_u}{\partial \ln T_u}(1-\sqrt{x})\frac{(T_u - T_w)}{T_u}\right]$$

$$C_i = -(v_{bi} - v_u)\frac{dx_{bi}}{d\theta} - v_{bi}\frac{\partial \ln v_{bi}}{\partial \ln T_{bi}}\frac{h_u - h_{bi}}{c_{pbi}T_{bi}}\left[\frac{dx_{bi}}{d\theta} - \frac{C}{\omega}x_{bi}(1-x)\right]$$

$$D_i = x_{bi}\left[\frac{v_{bi}^2}{c_{pb}T_{bi}}\left(\frac{\partial \ln v_{bi}}{\partial \ln T_{bi}}\right)^2 + \frac{v_{bi}}{p}\frac{\partial \ln v_{bi}}{\partial \ln p}\right]$$

$$E = (1-x)\left[\frac{v_u^2}{T_u c_{pu}}\left(\frac{\partial \ln v_u}{\partial \ln T_u}\right)^2 + \frac{v_u}{p}\frac{\partial \ln v_u}{\partial \ln p}\right]$$

Where :

- i is the suffix for the subdivided burning zone
- h_c is Woschni's coefficient where the enthalpy would be denoted as H
- x_{bi} is the current burning zone studied

Conclusion

This thesis first demonstrates the theoretical challenges of modifying a gasoline rotary engine (RE) to hydrogen (HRE). Given the specific characteristics of the engine, it has the potential to deliver excellent performance. This work focuses on the concentrations of nitric oxide in the exhaust gases. Indeed, RE emit less nitric oxide thanks to the strokes that expose the burned gases to the cooled in-housing walls for a significant longer time compared to reciprocating engines. Combined with the combustion characteristics of hydrogen, literature predicted less NO concentration in the exhaust gases for HRE than reciprocating HICE but more than gasoline rotary engines.

After analysing the results from the literature, this research has adapted Ferguson's two-zone homogeneous heat release model for a hydrogen rotary engine, considering various versions to understand the differences resulting from this conversion. This analysis concludes that the numerical model developed by Olikara and Borman is not suitable for computing the thermodynamic properties of the hot gas, limiting the calculations to the general combustion equation. In addition, the studies about the influence of Wiebe's burned fraction formula, the heat transfer coefficient and the gas leaks on this model demonstrate that this work could provide more accurate results after deep experimental research.

Following, an analysis concerning the influence of multiple parameters has been conduct. From this study, it came out that the equivalence ratio has the most significant impact on nitric oxide emission, followed by the angle of start of combustion and the engine speed, which its influence significantly differs from gasoline application. Finally, this research briefly go through the impact of engine boosting showing the hydrogen rotary engine still keeps its benefits on NO emissions.

In parallel with this work, a test bench was built to provide future measurements for research purposes, accompanied by detailed explanations about the building process.

In conclusion, Ferguson's Homogeneous Two-Zone Finite Energy Release model can

be adapted to a hydrogen rotary engine. However, experimental studies concerning pressure evolution, flame temperature, heat transfer, and gas leakage could improve this work by resolving the over-estimations provided by this model. Despite these needed improvements, many benefits of using hydrogen in rotary engines where observed regarding emissions reductions. Combined with potential further research on performance and exhaust treatment technologies, this engine could be a great application as a hydrogen internal combustion engine.

Bibliography

[1] F. LIU B. SUN J. DUAN. "NOx emission characteristics of hydrogen internal combustion engine". In: *JOURNAL OF BEIJING INSTITUTE OF TECHNOLOGY* 23(3) (2013), pp. 339–344. DOI: https://www.researchgate.net/publication/286554124_NOx_emission_characteristics_of_hydrogen_internal_combustion_engine.

[2] S. Gordon B.J. McBride and M.A. Reno. "Coefficients for Calculating Thermodynamic and Transport Properties of Individual Species". In: *NASA Technical Memorandum* (1993), p. 24.

[3] A. Kirkpatrick C. Ferguson. *Internal Combustion Engines : Applied Thermosciences*. 3. John Wiley Sons, Ltd, 2014. ISBN: 978-1-118-53331-4.

[4] C.Schwerdt. "Modelling NOx-Formation in Combustion Processes". In: 46 (2006). DOI: https://lup.lub.lu.se/luur/download?func=downloadFile&recordOId=8847808&fileOId=8859383.

[5] J. Clark. *Nitrogen and sulfur*. URL: https://www.chemguideforcie.co.uk/2022section12/learning12p1p1.html#:~:text=The%20nitrogen%20molecule%2C%20N2,%2B944%20kJ%20mol%2D1.. (accessed: 02.01.2024).

[6] P. Dimpelfeld and A. Humke. "Heat Release Characteristics of Stratified - Charge Rotary Engines". In: *SAE Transactions* 96 (1987), p. 10. DOI: https://www.jstor.org/stable/44718188.

[7] H. Jeanmart F. Contino. *Intake and Exhaust*. URL: https://moodle.uclouvain.be/pluginfile.php/120190/mod_resource/content/2/MECA2220_2021_cours07.pdf. (accessed: 08.02.2024).

[8] J. Heywood G. Danieli C. Ferguson and J. Keck. "Predicting the Emissions and Performance Characteristics of a Wankel Engine". In: *SAE Transactions* 83 (1974), p. 16. DOI: https://www.jstor.org/stable/44721432.

[9] J. Heywood G. Lavoie and J. Keck. "Experimental and Theoretical Study of Nitric Oxide Formation in Internal Combustion Engines". In: *Gordon and breach* 1 (1970), p. 13.

[10] C. Ji H. Wang. "Modeling and parametric study of the performance-emissions trade-off of a hydrogen Wankel rotary engine". In: *ScienceDirect* 318 (2022). DOI: https://doi.org/10.1016/j.fuel.2022.123662.

[11] J. B. Heywood and J. C. Keck. "Formation of Hydro- carbons and Oxides of Nitrogen in Automobile Engines." In: *Environmental Science Technology* 7 (1973), pp. 216–223. DOI: https://doi.org/10.1021/es60075a002.

[12] William L. Hosch. *Nikolaus Otto*. URL: https://www.britannica.com/biography/Nikolaus-Otto. (accessed: 08.02.2024).

[13] E. H. James. "Errors in NO Emission Prediction from Spark Ignition Engines". In: *SAE Technical Paper* (1982), p. 24. DOI: https://doi.org/10.4271/820046.

[14] C. Lee and H. Schock. "Regressed Relations for Forced Convection Heat Transfer in a Direct Injection Stratified Charge Rotary Engine". In: *NASA Technical Memorandum* (1988), p. 23. DOI: https://ntrs.nasa.gov/citations/19880003963.

[15] D. Musiał M. Zajemska A. Poskart. "The kinetics of nitrogen oxides formation in the flame gas". In: *Econstor* 15 (2015), pp. 445–460. DOI: http://hdl.handle.net/10419/178898.

[16] C. Olikara and G. Borman. "A Computer Program for Calculating Properties of Equilibrium Combustion Products with Some Applications to I.C. Engines". In: *SAE Technical Paper* (1975), p. 23. DOI: https://doi.org/10.4271/750468.

[17] D. J. Patterson and N. A. Henein. *Emissions from Combustion Engines and Their Control.* Michigan: Ann Arbor Science Publishers, 1972. ISBN: 9780250975143.

[18] Wrapped Perception. *See Thru Rotary Engine in Slow Motion - (Wankel Engine) 4K*. URL: https://www.youtube.com/watch?v=pCteBhr4dGY&t=480s&ab_channel=WarpedPerception. (accessed: 24.04.2024).

[19] J. Lockley R. Ansdale. "The Wankel RC Engine : design and performance". In: *London Ilife Books LTD* (1968), p. 170.

[20] G. Lavoie R. Miller G. Davis and T. Gardner. "A Super-Extended Zeldovich Mechanism for NOx Modeling and Engine Calibration". In: *SAE Transactions* 107 (1998), p. 11. DOI: https://www.jstor.org/stable/44736596.

[21] Full race. *THE GREAT DIVIDE | TWIN SCROLL VS. SINGLE SCROLL TURBO TEST*. URL: https://www.full-race.com/resources/articles/the-great-divide-%7C-twin-scroll-vs-single-scroll-turbo-test#:~:text=A%20twin%2Dscroll%20turbocharger%20system%20requires%20a%20divided%2Dinlet%20turbine,be%20teamed%20on%20one%20scroll.. (accessed: 25.04.2024).

[22] I.Yakovlev S.Zambalov and A. Maznoy. *Effect of multiple fuel injection strategies on mixture formation and combustion in a hydrogen-fueled rotary range extender for battery electric vehicles*. URL: https://www.researchgate.net/

figure/Schematic-diagram-of-the-rotary-engine_fig1_342346985. (accessed: 12.12.2023).
[23] J. Terrell. *Ultimate 13B Rotary Engine Guide*. URL: https://www.drifted.com/13b-engine/. (accessed: 10.04.2024).
[24] K. Thielen and P. Roth. "Resonance absorption measurements of N and O atoms in high temperature no dissociation and formation kinetics". In: *Elsevier* 20 (1985), p. 8. DOI: https://doi.org/10.1016/S0082-0784(85)80558-0.
[25] UK. *NITROGEN OXIDES FORMATION incombustionprocesses*. URL: http://fluid.wme.pwr.wroc.pl/~spalanie/dydaktyka/combustion_en/NOx/NOx_formation.pdf. (accessed: 21.12.2023).
[26] V. Vasistha. *What is the difference in pollution in the case of diesel and petrol engines?* URL: https://www.researchgate.net/post/What-is-the-difference-in-pollution-in-the-case-of-diesel-and-petrol-engines. (accessed: 12.01.2024).
[27] Wikipedia. *NOx*. URL: https://en.wikipedia.org/wiki/NOx. (accessed: 08.12.2023).
[28] G. Woschni. "A Universally Applicable Equation for the Instantaneous Heat Transfer Coefficient in the Internal Combustion Engine". In: *SAE Transactions* 76 (1978), p. 19. DOI: https://www.jstor.org/stable/44562845.
[29] K. Yamamoto. *Rotary engine*. Sankaido Co., 1981.

Appendix A

Computations

A.1 Equilibrium equation

$$H_b + \frac{\lambda}{2}(O_2 + 3.76N_2) \rightarrow \nu_1 H_2O + \nu_2 N_2 + \nu_3 O_2 + \nu_4 H_2 + \nu_5 H + \nu_6 O + \nu_7 NO + \nu_8 OH$$

The equation system from molecular balance is then,

$$\begin{cases} H: & b = 2\nu_1 + 2\nu_4 + \nu_5 + \nu_8 \\ O: & \lambda = \nu_1 + 2\nu_3 + \nu_6 + \nu_7 + \nu_8 \\ N: & 3.76\lambda = 2\nu_2 + \nu_7 \end{cases}$$

$$\begin{cases} H: & b = (2y_1 + 2y_4 + y_5 + y_8)N \\ O: & \lambda = (y_1 + 2y_3 + y_6 + y_7 + y_8)N \\ N: & 3.76\lambda = (2y_2 + y_7)N \end{cases}$$

By setting two constants,

$$\begin{cases} D_1 = \frac{\lambda}{b} \\ D_2 = \frac{3.76\lambda}{b} \end{cases}$$

The following three equations are combined with the mole fraction definition,

$$\begin{cases} f_0: & \sum_i y_i = 1 \\ f_1: & y_1 + 2y_3 + y_6 + y_7 + y_8 - D_1(2y_1 + 2y_4 + y_5 + y_8) = 0 \\ f_2: & 2y_2 + y_7 - D_2(2y_1 + 2y_4 + y_5 + y_8) = 0 \end{cases}$$

The system has three equations for eight unknowns. Therefore, the following rate of reactions from the equilibrium reaction introduced in section 2.3.2 are to be

considered, [3]

$$
\begin{array}{lll}
K_1 = \dfrac{y_5\sqrt{p}}{\sqrt{y_4}} & \dfrac{dc_1}{dt} = \dfrac{d}{dt}\left(\dfrac{K_1}{\sqrt{p}}\right) & \dfrac{dc_1}{dp} = -\dfrac{K_1}{2p^{3/2}} \\
K_2 = \dfrac{y_6\sqrt{p}}{\sqrt{y_3}} & \dfrac{dc_2}{dt} = \dfrac{d}{dt}\left(\dfrac{K_2}{\sqrt{p}}\right) & \dfrac{dc_2}{dp} = -\dfrac{K_2}{2p^{3/2}} \\
K_3 = \dfrac{y_8}{\sqrt{y_3 y_4}} & \dfrac{dc_3}{dt} = \dfrac{dK_3}{dt} & \dfrac{dc_3}{dp} = 0 \\
K_4 = \dfrac{y_7}{\sqrt{y_2 y_3}} & \dfrac{dc_4}{dt} = \dfrac{dK_4}{dt} & \dfrac{dc_4}{dp} = 0 \\
K_5 = \dfrac{y_1}{y_4\sqrt{y_3}\sqrt{p}} & \dfrac{dc_5}{dt} = \dfrac{d}{dt}(K_5\sqrt{p}) & \dfrac{dc_5}{dp} = 2K_2 p^{3/2}
\end{array}
$$

By knowing K_i thanks to the table in Appendix B.1, the system is computed by constructing the Jacobian matrix defined as,

$$
J = \begin{pmatrix} \frac{\partial f_0}{\partial x_0} & \cdots & \frac{\partial f_0}{\partial x_n} \\ \cdots & \cdots & \cdots \\ \frac{\partial f_m}{\partial x_0} & \cdots & \frac{\partial f_m}{\partial x_n} \end{pmatrix}
$$

By computing each derivative and setting the parameter $d_{ij} = \frac{\partial y_i}{\partial y_j}$,

$$
\begin{pmatrix}
1 + d_{72} & 1 + M_1 & 1 + M_2 + d_{54} \\
d_{72} & 2 + M_1 - 2D_1 d_{13} - D_1 d_{83} & M_2 - 2D_1 d_{14} - 2D_1 - D_1 d_{54} - D_1 d_{84} \\
2 + d_{72} & d_{73} - 2 * D_2 d_{13} - D_2 d_{83} & -2D_2 d_{14} - 2D_2 - D_2 d_{54} - D_2 d_{84}
\end{pmatrix}
$$

Where,

$$
\begin{aligned}
M_1 &= d_{13} + d_{63} + d_{73} + d_{83} \\
M_2 &= d_{14} + d_{84}
\end{aligned}
$$

Now compute y_2, y_3 and y_4 are computed by iteration and by resolving the matrix equation with the *maximum pivot Gaussian elimination routine*,

$$
Jy = \begin{pmatrix}
-(y_1 + y_2 + y_3 + y_4 + y_5 + y_6 + y_7 + y_8 - 1) \\
-(y_1 + 2y_3 + y_6 + y_7 + y_8 - 2D_1 y_1 - 2D_1 y_4 - D_1 y_5 - D_1 y_8) \\
-(2y_2 + y_7 - 2D_2 y_1 - 2D_2 y_4 - D_2 y_5 - D_2 y_8)
\end{pmatrix}
$$

To compute the evolution of the thermodynamic properties as the reaction operates, the rate of the molar fraction according to time, dy/dt, and pressure, dy/dp are needed. They are obtained by resolving the two other matrix equations.

$$J\frac{dy}{dt} = \begin{pmatrix} \frac{dc_5}{dt}x_1 + \frac{dc_1}{dt}x_5 + \frac{dc_2}{dt}x_6 + \frac{dc_4}{dt}x_7 + \frac{dc_3}{dt}x_8 \\ \frac{dc_5}{dt}x_1 + \frac{dc_2}{dt}x_6 + \frac{dc_3}{dt}x_8 + \frac{dc_4}{dt}x_7 - 2D_1\frac{dc_5}{dt}x_1 - D_1x_5\frac{dc_1}{dt} - D_1x_8\frac{dc_3}{dt} \\ \frac{dc_4}{dt}x_7 - 2D_2\frac{dc_5}{dt}x_1 - D_2x_5\frac{dc_1}{dt} - D_2x_8\frac{dc_3}{dt} \end{pmatrix}$$

$$J\frac{dy}{dp} = \begin{pmatrix} \frac{dc_5}{dp}x_1 + \frac{dc_1}{dp}x_5 + \frac{dc_2}{dp}x_6 \\ \frac{dc_5}{dp}x_1 + \frac{dc_2}{dp}x_6 - 2D_1x_1\frac{dc_5}{dp} - D_1x_5\frac{dc_1}{dp} \\ -2D_2x_1\frac{dc_5}{dp} - D_2x_5\frac{dc_1}{dp} \end{pmatrix}$$

With these equations, dy_i/dt and dy_i/dp for $i = 2, 3$ and 4 are found. The last computation to make for the thermodynamic properties are,

$$\frac{dy}{dt} = \begin{pmatrix} y_4\sqrt{y_3}\frac{dc_5}{dt} + d_{13}\frac{dy_3}{dt} + d_{14}\frac{dy_4}{dt} \\ \frac{dy_2}{dt} \\ \frac{dy_3}{dt} \\ \frac{dy_4}{dt} \\ \sqrt{y_4}\frac{dc_1}{dt} + d_{54}\frac{dy_4}{dt} \\ \sqrt{y_3}\frac{dc_2}{dt} + d_{63}\frac{dy_3}{dt} \\ \sqrt{y_2y_3}\frac{dc_4}{dt} + d_{72}\frac{dy_2}{dt} + d_{73}\frac{dy_3}{dt} \\ \sqrt{y_3y_4}\frac{dc_3}{dt} + d_{83}\frac{dy_3}{dt} + d_{84}\frac{dy_4}{dt} \end{pmatrix} \quad \frac{dy}{dp} = \begin{pmatrix} y_4\sqrt{y_3}\frac{dc_5}{dp} + d_{13}\frac{dy_3}{dp} + d_{14}\frac{dy_4}{dp} \\ \frac{dy_2}{dp} \\ \frac{dy_3}{dp} \\ \frac{dy_4}{dp} \\ \sqrt{y_4}\frac{dc_1}{dp} + d_{54}\frac{y_4}{dp} \\ \sqrt{y_3}\frac{dc_2}{dp} + d_{63}\frac{dy_3}{dp} \\ d_{72}\frac{dy_2}{dp} + d_{73}\frac{dy_3}{dp} \\ d_{83}\frac{dy_3}{dp} + d_{84}\frac{dy_4}{dp} \end{pmatrix}$$

A.2 Homogeneous Two-zones heat released

$$\frac{dQ}{d\theta} - p\frac{dV}{d\theta} = \frac{dU}{d\theta} \tag{A.1}$$

Specific volume

The specific volume is introduced as,

$$v = \frac{V}{m} = xv_b + (1-x)v_u \tag{A.2}$$

By taking the derivative of equation A.2,

$$\frac{1}{m}\frac{dV}{d\theta} = x\frac{dv_b}{d\theta} + (1-x)\frac{dv_u}{d\theta} + (v_b - v_u)\frac{dx}{d\theta} \tag{A.3}$$

Where the variations of v_b and v_u according to θ are :

$$\frac{dv_i}{d\theta} = \frac{\partial v_i}{\partial T_i}\frac{dT_i}{d\theta} + \frac{\partial v_i}{\partial p}\frac{dp}{d\theta} \tag{A.4}$$

Where $i = u$ *or* b for burned or unburned gases. After incorporating equation A.4 in A.3,

$$\frac{1}{m}\frac{dV}{d\theta} = x\frac{\partial v_b}{\partial T_b}\frac{dT_b}{d\theta} + (1-x)\frac{\partial v_u}{\partial T_u}\frac{dT_u}{d\theta} + \left[x\frac{\partial v_b}{\partial p} + (1-x)\frac{\partial v_u}{\partial p}\right]\frac{dp}{d\theta} + (v_b - v_u)\frac{dx}{d\theta} \tag{A.5}$$

Specific internal energy

Similarly to the specific volume,

$$u = \frac{U}{m} = xu_b + (1-x)u_u \tag{A.6}$$

By taking the derivative of the two specific internal energy,

$$\frac{\partial u_i}{\partial \theta} = \frac{\partial u_i}{\partial T_i}\frac{dT_i}{d\theta} + \frac{\partial u_i}{\partial p}\frac{dp}{d\theta} \tag{A.7}$$

$$= \left(c_{pi} - p\frac{\partial v_i}{\partial T_i}\right)\frac{dT_i}{d\theta} - \left(T_i\frac{\partial v_i}{\partial T_i} + \frac{\partial v_i}{\partial p}\right)\frac{dp}{d\theta} \tag{A.8}$$

By incorporating equation A.8 in the derivative of equation A.6,

$$\begin{aligned} m\frac{du}{d\theta} =& mx(c_{pb} - p\frac{\partial v_b}{\partial T_b})\frac{dT_b}{d\theta} + m(1-x)(c_{pu} - p\frac{\partial v_u}{\partial T_u})\frac{dT_u}{d\theta} \\ &- \left[mx\left(T_b\frac{\partial v_b}{\partial T_b} + p\frac{\partial v_b}{\partial p}\right) + m(1-x)\left(T_u\frac{\partial v_u}{\partial T_u} + p\frac{\partial v_u}{\partial p}\right)\right]\frac{dp}{d\theta} \\ &+ m(u_b - u_u)\frac{dx}{d\theta} \end{aligned} \tag{A.9}$$

Heat losses

By adding the heat losses further developed in section 2.7.2,

$$\frac{dQ}{d\theta} = -\frac{\dot{Q}_b + \dot{Q}_u}{\omega} \tag{A.10}$$

$$\dot{Q}_b = hA_b(T_b - T_w) \tag{A.11}$$

$$\dot{Q}_u = hA_u(T_u - T_w) \tag{A.12}$$

Where $h = h_u = h_b$ is the convection heat coefficient and, A_b and A_u are the areas in contact with the chamber walls. These areas are divided as,

$$A_b = A_c\sqrt{x} \tag{A.13}$$
$$A_u = A_c(1 - \sqrt{x}) \tag{A.14}$$

The dependency on the square root of the burned mass fraction is explained by the density difference between the two gases. The burned gases occupies more space. To be more accurate, the exponent should vary according to experimental analysis but in theory it is a good approximation to set the exponent to 1/2. [3]

However, in order to have enough equations, entropy is introduced,

$$\frac{\partial s_i}{\partial \theta} = \frac{\partial s_i}{\partial T_i}\frac{dT_i}{d\theta} + \frac{\partial s_i}{\partial p}\frac{dp}{d\theta} = \frac{c_{pi}}{T_i}\frac{dT_i}{d\theta} + \frac{\partial v_i}{\partial T_i}\frac{dp}{d\theta} \tag{A.15}$$

Then the relations, for $i = u$ *or* b become,

$$c_{pi}\frac{T_i}{d\theta} - T_i\frac{\partial v_i}{\partial T_i}\frac{dp}{d\theta} = -\frac{hA_i}{\omega m(1-x)}(T_i - T_w) \tag{A.16}$$

Equation system

By incorporating in A.1 equations A.5, A.9, A.10 and A.16, the following equation system is obtained,

$$\frac{dp}{d\theta} = \frac{A + B + C}{D + E} \tag{A.17}$$
$$\frac{dT_b}{d\theta} = \frac{-hA_c(T_b - T_w)}{\omega m c_{pb}\sqrt{x}} + \frac{T_b}{c_{pb}}\frac{\partial v_b}{\partial T_b}\frac{A + B + C}{D + E} + \frac{h_u - h_b}{xc_{pb}}\frac{dx}{x\theta} \tag{A.18}$$
$$\frac{dT_u}{d\theta} = \frac{-hA_c(1 - x^2)(T_u - T_w)}{\omega m c_{pu}(1-x)} + \frac{T_u}{c_{pu}}\frac{\partial v_u}{\partial T_u}\frac{A + B + C}{D + E} \tag{A.19}$$

Where the coefficient A, B, C, D and E are,

$$A = \frac{1}{m}\frac{dV}{d\theta} \tag{A.20}$$
$$B = \frac{hA_c}{\omega m}\left[\frac{1}{c_{pb}}\frac{\partial v_b}{\partial T_b}\sqrt{x}(T_b - T_w) + \frac{1}{c_{pu}}\frac{\partial v_u}{\partial T_u}(1 - \sqrt{x})(T_u - T_w)\right] \tag{A.21}$$
$$C = -(v_b - v_u)\frac{dx}{d\theta} - \frac{\partial v_b}{\partial T_b}\frac{h_u - h_b}{c_{pb}}\frac{dx}{d\theta} \tag{A.22}$$
$$D = x\left[\frac{T_b}{c_{pb}}\left(\frac{\partial v_b}{\partial T_b}\right)^2 + \frac{\partial v_b}{\partial p}\right] \tag{A.23}$$
$$E = (1 - x)\left[\frac{T_u}{c_{pu}}\left(\frac{\partial v_u}{\partial T_u}\right)^2 + \frac{\partial v_u}{\partial p}\right] \tag{A.24}$$

A.3 Simulation python code

The python code for the hole programming is at the following link : `https://github.com/Ranger2004/HydrogenWankel.git`

Appendix B

Molecular properties

B.1 Constant equilibrium factors

The temperature dependent constant equilibrium for the reactions listed in section 2.3.2 respond to the equation,[3]

$$\log_{10} K_i(T) = A_i \ln\left(\frac{T}{1000}\right) + \frac{B_i}{T} + C_i + D_i T + E_i T^2 \tag{B.1}$$

K_i	A_i	B_i	C_i	D_i	E_i
K_1	$+0.432168E+00$	$-0.112464E+05$	$+0.267269E+01$	$-0.745744E-04$	$+0.242484E-08$
K_2	$+0.310805E+00$	$-0.129540E+05$	$+0.321779E+01$	$-0.738336E-04$	$+0.344645E-08$
K_3	$-0.141784E+00$	$-0.213308E+04$	$+0.853461E+00$	$+0.355015E-04$	$-0.310227E-08$
K_4	$+0.150879$	$-0.470959E+04$	$+0.646096E+00$	$+0.272805E-05$	$-0.154444E-08$
K_5	$-0415302E-02$	$+0.148627E+05$	$-0475746E+01$	$+0.124699E-03$	$-0.900227E-08$

Table B.1: Equilibrium Constant K_i Curve-Fit Coefficient[3]

B.2 Curve-Fit table

The thermodynamic properties follows the empirical equations,

$$\frac{C_p(T)}{R} = a_1 + a_2 T + a_3 T^2 + a_4 T^3 + a_5 T^4 \tag{B.2}$$

$$\frac{H_p(T)}{RT} = a_1 + a_2\frac{T}{2} + a_3\frac{T^2}{3} + a_4\frac{T^3}{4} + a_5\frac{T^4}{5} + \frac{b_1}{T} \tag{B.3}$$

$$\frac{S(T)}{R} = a_1 \ln T + +a_2 T + a_3\frac{T^2}{2} + a_4\frac{T^3}{3} + a_5\frac{T^4}{4} + b_2 \tag{B.4}$$

The thermodynamic coefficients are listed in Figure B.1.[2]

Record	Contents	Format	Columns
1	Species name	A15	1–15
	Reference/date code	A6	19–24
	Chemical formula: symbols and numbers	4 (A2, F3.0)	25–44
	"G" for gaseous species, "C" for condensed	A1	45
	Temperature range	2F10.3	46–65
	Molecular weight	F13.5	66–78
	Integer 1	I1	80
2	Coefficients $a_i (i = 1,5)$ in eq. (1) for $T \geq 1000$ K	5E15.8	1–75
	Integer 2	I1	80
3	Coefficients b_1 and b_2 in eqs. (2) and (3) for $T \geq 1000$ K	2E15.8	1–30
	Coefficients a_i $(i = 1,3)$ in eq. (1) for $T \leq 1000$ K	3E15.8	31–75
	Integer 3	I1	80
4	Coefficients a_i $(i = 4,5)$ in eq. (1) for $T \leq 1000$ K	2E15.8	1–30
	Coefficients b_1 and b_2 in eqs. (2) and (3) for $T \leq 1000$ K	2E15.8	31–60
	$H^o(298.15)/R$, K	E15.8	61–75
	Integer 4	I1	80

```
H                 L 5/93H  1.   0.   0.   0.G   200.000  6000.000      1.00794 1
 2.50000286E+00-5.65334214E-09 3.63251723E-12-9.19949720E-16 7.95260746E-20    2
 2.54736589E+04-4.46698494E-01 2.50000000E+00 0.00000000E+00 0.00000000E+00    3
 0.00000000E+00 0.00000000E+00 2.54736599E+04-4.46682853E-01 2.62190349E+04    4
H2                TPIS78H  2.   0.   0.   0.G   200.000  6000.000      2.01588 1
 2.93286579E+00 8.26607967E-04-1.46402335E-07 1.54100359E-11-6.88804432E-16    2
-8.13065597E+02-1.02432887E+00 2.34433112E+00 7.98052075E-03-1.94781510E-05    3
 2.01572094E-08-7.37611761E-12-9.17935173E+02 6.83010238E-01 0.00000000E+00    4
H20               L 8/89H  2.0  1.   0.   0.G   200.000  6000.000     18.01528 1
 2.67703787E+00 2.97318329E-03-7.73769690E-07 9.44336689E-11-4.26900959E-15    2
-2.98858938E+04 6.88255571E+00 4.19864056E+00-2.03643410E-03 6.52040211E-06    3
-5.48797062E-09 1.77197817E-12-3.02937267E+04-8.49032208E-01-2.90848168E+04    4
NO                TPIS89N  1.0  1.   0.   0.G   200.000  6000.000     30.00614 1
 3.26071234E+00 1.19101135E-03-4.29122646E-07 6.94481463E-11-4.03295681E-15    2
 9.92143132E+03 6.36900518E+00 4.21859896E+00-4.63988124E-03 1.10443049E-05    3
-9.34055507E-09 2.80554874E-12 9.84509964E+03 2.28061001E+00 1.09770882E+04    4
N2                TPIS78N  2.   0.   0.   0.G   200.000  6000.000     28.01348 1
 2.95257626E+00 1.39690057E-03-4.92631691E-07 7.86010367E-11-4.60755321E-15    2
-9.23948645E+02 5.87189252E+00 3.53100528E+00-1.23660987E-04-5.02999437E-07    3
 2.43530612E-09-1.40881235E-12-1.04697628E+03 2.96747468E+00 0.00000000E+00    4
O                 L 1/90O  1.   0.   0.   0.G   200.000  6000.000     15.99940 1
 2.54363697E+00-2.73162486E-05-4.19029520E-09 4.95481845E-12-4.79553694E-16    2
 2.92260120E+04 4.92229457E+00 3.16826710E+00-3.27931884E-03 6.64306396E-06    3
-6.12806624E-09 2.11265971E-12 2.91222592E+04 2.05193346E+00 2.99687009E+04    4
OH                TPIS78O  1.H  1.   0.   0.G   200.000  6000.000     17.00734 1
 2.83864607E+00 1.10725586E-03-2.93914978E-07 4.20524247E-11-2.42169092E-15    2
 3.94395852E+03 5.84452662E+00 3.99201543E+00-2.40131752E-03 4.61793841E-06    3
-3.88113333E-09 1.36411470E-12 3.61508056E+03-1.03925458E-01 4.73234213E+03    4
O2                TPIS89O  2.   0.   0.   0.G   200.000  6000.000     31.99880 1
 3.66096083E+00 6.56365523E-04-1.41149485E-07 2.05797658E-11-1.29913248E-15    2
-1.21597725E+03 3.41536184E+00 3.78245636E+00-2.99673415E-03 9.84730200E-06    3
-9.68129508E-09 3.24372836E-12-1.06394356E+03 3.65767573E+00 0.00000000E+00    4
```

Figure B.1: Thermodynamic coefficients

Appendix C

The test bench

This appendix regroup the construction process undertaken in the laboratory in order to make the engine work under gasoline and hydrogen fuel. This engine will further be used in laboratory courses for the Catholic University of Louvain.

C.1 Engine condition and challenges

The engine is a water-cooled, Mazda 13B-T from a Mazda FC3S S5 Turbo RX-7 Turbo-II dated between 1989 and 1991. Having two rotors with a total displacement of 1.3 $[l]$ and a compression ratio of 9.0 : 1, this engine delivers a power of 147 $[kW]$ at 6500 $[RPM]$ and a torque of 265 $[Nm]$ at 3500 $[RPM]$. [23]

The engine has been retaken from another project. It has been then already disassembled, tested part by part and reassembled. At first sight, the next steps of the project are to be identified,

1. Engine inspection for reassembly default
2. water cooling system installation
3. lubricating system installation
4. braking system development and installation
5. drive-by-wire throttle body adaptation
6. hydrogen supply design and installation
7. Electronic Control Unit (ECU) tuning

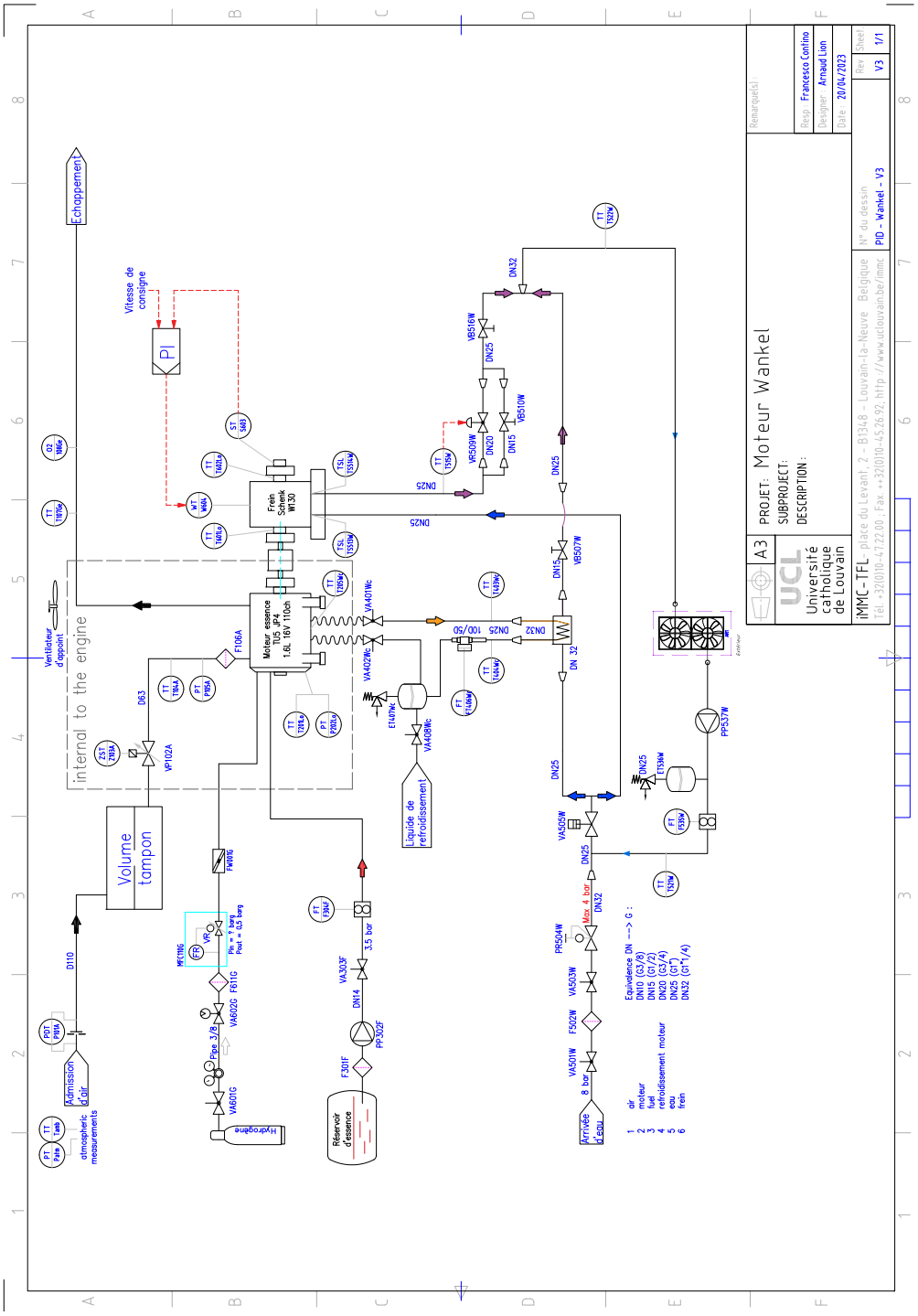

Figure C.1: P&ID of the bench

C.2 Engine inspection

Retaking an engine from a project started by someone else requires more attention because the person skills and their work quality are unknown. Therefore, a first inspection is set to search for poorly screwed bolts and verifying the engine parts bought. Multiple loss bolts were identified creating oil and water leaks located at the oil carter, the oil supply at the turbocharger, heat exchangers, ...

After tighten the bolts again to prevent further leaks, the next engine part to take care is the starter. As known, Mazda produced powerless starter making the engine hard to start at engine speeds close to 150 $[RPM]$ because of a power close to 1.2 $[kW]$. To compensate this lack of power, an updated version was delivered with a power of 2.2 $[kW]$ making the engine reach 300 $[RPM]$.

C.3 Water cooling system

The Mazda 13B-T is a water cooled engine. For the experiment bench,modifications were set up to simulate the water cycle in the car. In the RX7, the water is stored in the reservoir then circulates, thanks to the water pump, inside the housing to first accumulate the engine heat close to the TDC. The water passes then close the intake and exhaust ports before accessing the radiator were the water is cooled by air from two sources, the air coming through the front grille of the car and the fan directly fixed on the crankshaft (cfr. Figure C.2).

The engine in the laboratory is standing on a bench and the radiator grille is not usable due to its condition. Therefore, the radiator heat exchanger were replaced by an water-water heat exchanger connected to tap water (cfr. Figure C.1).

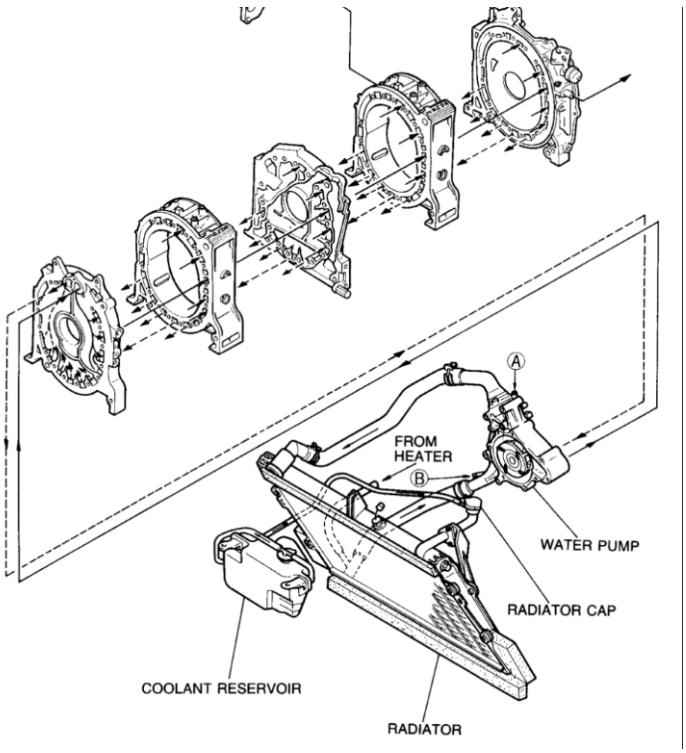

Figure C.2: Original water circuit

C.4 Oil system

To lubricate the engine, oil is used and circulates thanks to the oil pump (n°1 in figure C.3). The quantity of oil that will be injected in the housing is managed by the *oil metering pump*, OMP, (n°7). The OMP opening is managed by the ECU after reading the manifold pressure and the rotation speed of the engine by following the table C.1. To ensure the cooling of oil, it passes through a small radiator air-oil heat exchanger. As all engine, before the oil is used in the engine, it is pumped through the filter (n°5). After that, the oil goes pass either the turbocharger (n°10), the bearings, the CAS, the rotor or the oil injectors (n°8 and n°9).

By circulating inside the engine, the oil accumulates heat and need to be cooled. In the original RX7, the oil passes through a radiator grille placed in front of the car and is cooled by air the same way explained for the water coolant (cfr. Section C.3). However, for the laboratory application, the oil radiator grille was switched with an water-oil heat exchanger directly connected to the water coolant system (cfr. Figure C.1).

Pressure	500	1000	2000	4000	6000	8000
250	48	51	57	69	80	90
200	43	44	50	60	71	80
150	38	39	43	51	60	68
100	31	32	34	37	42	48
80	22	22	26	30	34	38
60	22	22	22	22	24	26

Table C.1

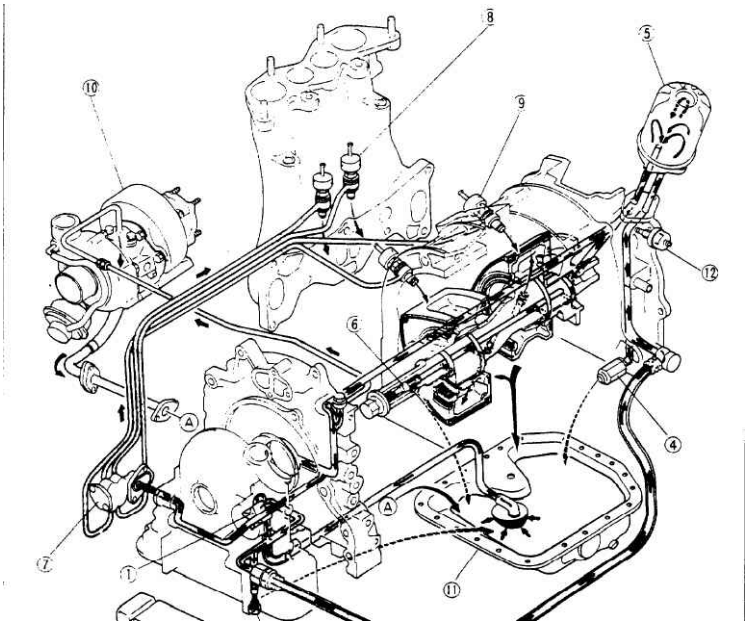

Figure C.3: Original oil circuit

C.5 Throttle control

Originally, the throttle valve of the Mazda RX7 is managed by a throttle cable. In this application, the throttle should be managed with the ECU to facilitate its control with the panel. Therefore, the original throttle plates were removed and a drive-by-wire has been placed, between the old throttle body position and the after the intercooler, the body directly connected to the ECU.

The Citroën C3, C4 and Peugeot 307 throttle models, *BOSH* 0280750085, has been selected using the connections illustrated in figure C.4

A) Bosch 0280750085

Peugeot 307/Citroen C3,C4	Pin	Func.	Pin	Func.
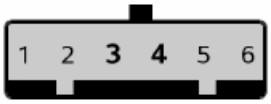	1	Coil+	4	TPS2
	2	Coil-	5	5V
	3	GND	6	TPS1

Figure C.4: Throttle body electronic connections

C.6 Braking system

An eddy current brake (cfr. Figure C.5) is used to simulate engine load. This braking system is an electromagnetic type that uses the principles of electromagnetic induction to generate braking force. It's a non-contact braking mechanism, meaning there is no physical contact between the braking components, which can lead to reduced wear and maintenance.

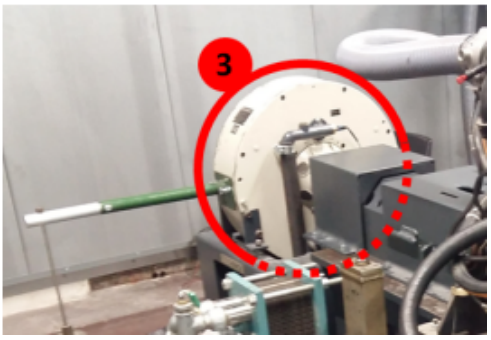

Figure C.5: Eddy current brake

C.7 Hydrogen feeding system

The engine is powered by gasoline and hydrogen as designed in the P&ID (cfr. Figure C.1). The point is to transit from gasoline to hydrogen while the engine is running. Therefore, the gasoline and hydrogen feeding system are managed by the **LabView** system where the debt of gasoline and hydrogen are given to us.

The supply system of hydrogen is equipped with a security valve and a back fire protecting system. To identify the flow meter and the section of the supply conduct, the hydrogen flow is computed as,

$$\dot{V}_{H_2} = \frac{273.15}{101325} \frac{p_1 V_d}{T_1} \frac{\Omega}{2} 1000 \; [Nl/min] \tag{C.1}$$

From this value, the section of the supply conduit and the flow meter adapted for this application can be computed.

C.8 M130 Electronic Control Unit

C.8.1 Engine calibration

The configuration of the ECU MoTeC M130 is at the following link: `https://github.com/Ranger2004/HydrogenWankel.git`

C.8.2 Ignition system

Each rotor is equipped with two sparks, the trailing (TS) and the leading spark (LS). The leading spark is responsible for the correct combustion of the fresh gases and the trailing ensure the complete combustion. Because the trailing spark needs less energy, its cavity access to the inside housing is smaller than the leading spark one (cfr. Figure C.6a). The ECU's ignition map controls the LS and the TS is managed either by a split table or basic table depending on the type of ECU used.

The Figure C.7 show the ignition coils and igniter wiring. The RX7 engine is not a direct ignition system because the leading sparks of each rotors shares the same coil inducing a dead spark. Indeed, the two rotors are shifted by 180 crankshaft degrees. Therefore, in both rotors, there is a spark every 180 degrees of the crankshaft. This method does not change in the performances of the engine but allows it to avoid the complexity of leading spark synchronisation.

(a) Leading and Trailing spark opening

(b) Spark model used as trailing and leading

Figure C.6: Spark system parts of the engine

RPM/MAP	0	500	750	1000	1250	1500	2000	2500	3000	3500	4000
0 $[kPa]$	0.0	5.0	5.0	5.0	7.4	10.0	18.0	27.0	28.0	29.0	31.0
20 $[kPa]$	0.0	5.0	5.0	5.0	7.4	10.0	18.0	25.0	27.6	28.6	30.6
40 $[kPa]$	0.0	5.0	5.0	5.0	7.4	10.0	18.0	24.2	27.0	28.0	30.2
60 $[kPa]$	0.0	5.0	5.0	5.0	7.4	10.0	18.0	23.6	26.2	27.6	29.6
80 $[kPa]$	0.0	5.0	5.0	5.0	7.4	10.0	14.0	23.0	26.0	27.2	28.8
90 $[kPa]$	0.0	5.0	5.0	5.0	5.0	7.4	12.4	20.4	23.4	24.6	26.4
100 $[kPa]$	0.0	5.0	5.0	5.0	5.0	7.0	11.0	18.0	20.0	22.0	24.0
120 $[kPa]$	0.0	0.0	1.4	3.0	3.6	5.2	8.6	14.8	17.0	19.0	20.8
140 $[kPa]$	0.0	0.0	0.4	1.0	1.2	2.8	6.2	11.6	14.0	16.0	17.6
160 $[kPa]$	0.0	0.0	0.0	0.0	0.0	0.0	4.0	9.0	11.8	13.6	15.2
180 $[kPa]$	0.0	0.0	0.0	0.0	0.0	0.0	2.0	7.4	10.4	12.2	13.6
200 $[kPa]$	0.0	0.0	0.0	0.0	0.0	0.0	0.0	5.6	9.0	10.6	11.2
220 $[kPa]$	0.0	0.0	0.0	0.0	0.0	0.0	0.0	4.4	7.2	8.4	9.8
240 $[kPa]$	0.0	0.0	0.0	0.0	0.0	0.0	0.0	3.4	5.4	6.4	7.2
260 $[kPa]$	0.0	0.0	0.0	0.0	0.0	0.0	0.0	2.2	3.6	4.2	4.8
280 $[kPa]$	0.0	0.0	0.0	0.0	0.0	0.0	0.0	1.0	1.8	2.0	2.4
300 $[kPa]$	0.0	0.0	0.0	0.0	0.0	0.0	0.0	0.6	0.8	1.0	1.2

Table C.2: Main ignition Map (part 1)

RPM/MAP	4500	5000	5500	6000	6500	7000	7500	8000	8500	9000
0 $[kPa]$	32.0	34.0	35.0	36.0	38.0	40.0	40.0	40.0	40.0	40.0
20 $[kPa]$	31.6	33.6	34.6	35.6	37.4	39.0	39.0	39.0	39.0	39.0
40 $[kPa]$	31.2	33.2	34.2	35.2	36.4	37.8	37.8	37.8	37.8	37.8
60 $[kPa]$	30.6	32.6	33.6	34.6	35.6	36.6	36.6	36.6	36.6	36.6
80 $[kPa]$	30.2	31.8	32.8	33.8	35.0	36.0	36.0	36.0	36.0	36.0
90 $[kPa]$	27.4	28.8	30.2	31.0	32.0	33.0	33.0	33.0	33.0	33.0
100 $[kPa]$	24.8	25.8	27.6	28.4	29.2	30.0	30.0	30.0	30.0	30.0
120 $[kPa]$	22.6	23.6	25.2	25.8	26.4	27.2	27.2	27.2	27.2	27.2
140 $[kPa]$	20.2	21.6	22.8	23.2	23.8	24.4	24.4	24.4	24.4	24.4
160 $[kPa]$	18.0	19.4	20.4	20.8	21.2	21.6	21.6	21.6	21.6	21.6
180 $[kPa]$	15.8	17.2	17.8	18.2	18.4	18.8	18.8	18.8	18.8	18.8
200 $[kPa]$	12.6	14.2	14.4	14.6	15.2	15.4	15.4	15.4	15.4	15.4
220 $[kPa]$	10.8	12.2	12.2	12.4	12.8	13.2	13.2	13.2	13.2	13.2
240 $[kPa]$	8.2	9.0	9.2	9.4	9.4	9.6	9.6	9.6	9.6	9.6
260 $[kPa]$	5.4	6.0	6.2	6.2	6.2	6.4	6.4	6.4	6.4	6.4
280 $[kPa]$	2.6	3.0	3.0	3.2	3.2	3.2	3.2	3.2	3.2	3.2
300 $[kPa]$	1.4	1.4	1.6	1.6	1.6	1.6	1.6	1.6	1.6	1.6

Table C.3: Main ignition Map (part 2)

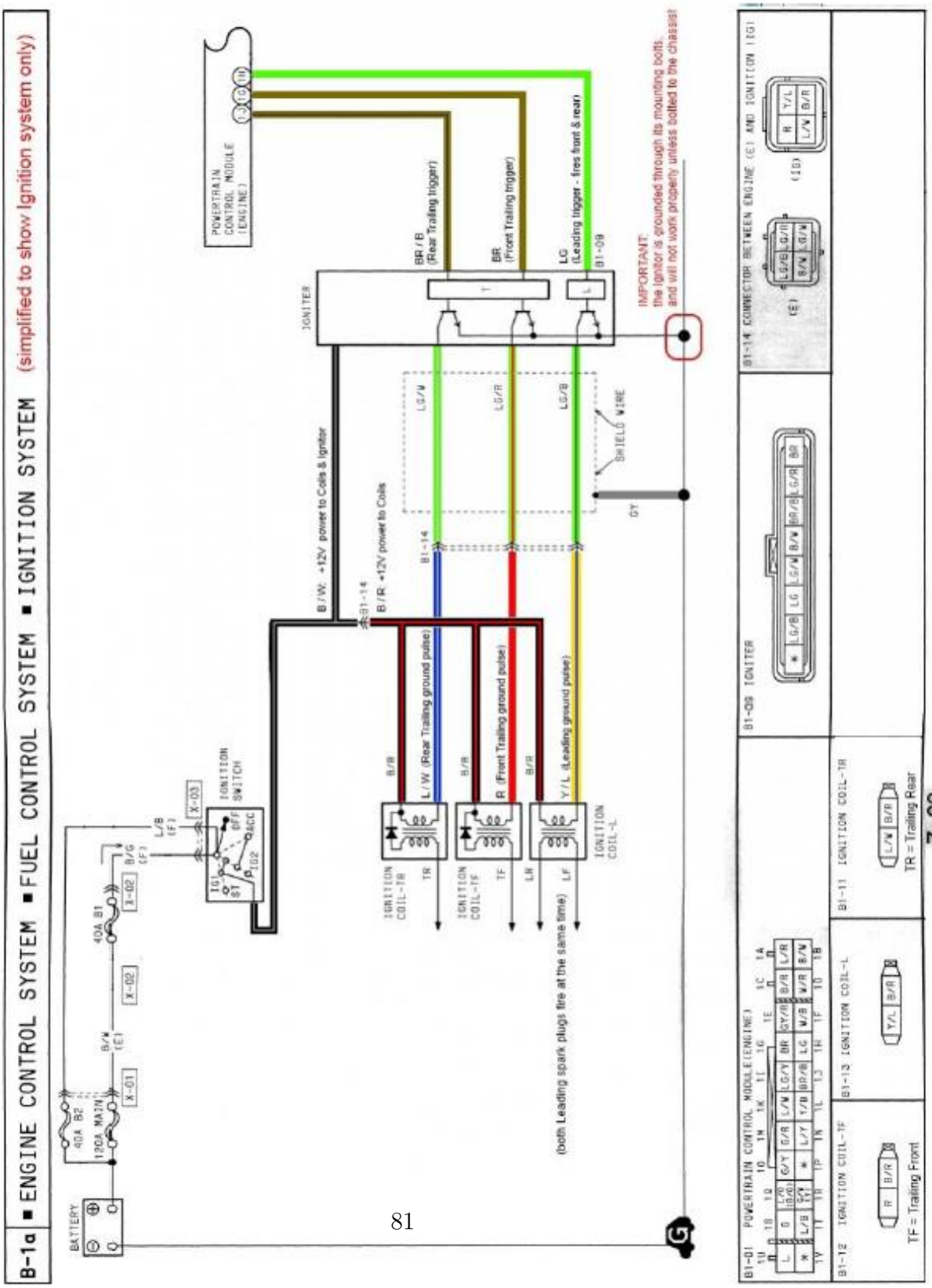
B-1a ■ ENGINE CONTROL SYSTEM ■ FUEL CONTROL SYSTEM ■ IGNITION SYSTEM (simplified to show Ignition system only)
BATTERY
120A MAIN
40A B2
40A B1
B/W (E1)
B/G (F)
L/B (F)
X-01
X-02
X-02
X-03
IGNITION SWITCH
OFF
ACC
IG2
IG1
ST
POWERTRAIN CONTROL MODULE (ENGINE)
IGNITER
BR/B (Rear Trailing trigger)
BR (Front Trailing trigger)
LG (Leading trigger - fires front & rear)
B1-09
B/W: +12V power to Coils & Ignitor
B/R: +12V power to Coils
B1-14
LG/W
LG/R
LG/B
SHIELD WIRE
GY
IMPORTANT:
the Ignitor is grounded through its mounting bolts,
and will not work properly unless bolted to the chassis
B/R
L/W (Rear Trailing ground pulse)
R (Front Trailing ground pulse)
Y/L (Leading ground pulse)
IGNITION COIL-TR
IGNITION COIL-TF
IGNITION COIL-L
TR
TF
LR
LF
(both Leading spark plugs fire at the same time)
B1-01 POWERTRAIN CONTROL MODULE (ENGINE)
B1-09 IGNITER
B1-14 CONNECTOR BETWEEN ENGINE (E) AND IGNITION (IG1)
B1-12 IGNITION COIL-TF
B1-13 IGNITION COIL-L
B1-11 IGNITION COIL-TR
TF = Trailing Front
TR = Trailing Rear
Z-28

Figure C.7

C.8.3 Injection system

Each rotor of the engine are equipped with two fuel injectors. The secondary injector is responsible to compensate the main injector in high speed. However, the ECU has a predefined map for the main injector, the secondary does not have one. The ECU, with the informations provide on the main injector, identifies to quantity of fuel that it can injects compared to the fuel quantity needed. If it seems that there is too much fuel to injects compared to the time, then the ECU will share out the fuel quantity between the two injectors.

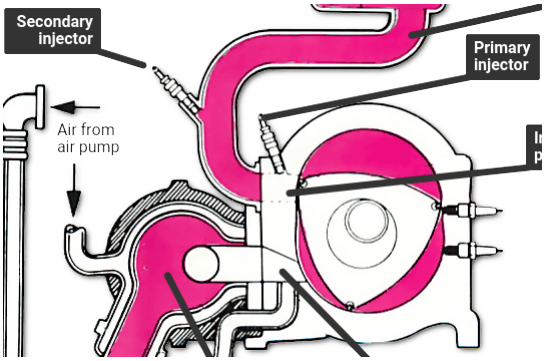

Figure C.8

RPM/MAP	0	250	500	750	1000	1250	1500	2000	2500	3000
0 $[kPa]$	18.34	20.34	20.34	21.96	24.04	26.04	24.20	26.04	25.84	26.52
20 $[kPa]$	31.34	33.34	33.34	36.30	38.14	41.00	40.52	43.28	45.28	46.96
40 $[kPa]$	51.62	53.62	56.00	59.00	60.00	63.00	59.94	61.94	68.36	69.94
50 $[kPa]$	56.00	58.00	58.00	61.00	62.00	66.00	66.94	70.46	78.16	79.98
60 $[kPa]$	59.98	61.98	66.00	69.00	72.00	75.00	75.56	76.30	81.42	82.44
80 $[kPa]$	68.36	70.36	74.00	77.00	82.00	80.00	80.46	78.26	85.36	87.84
100 $[kPa]$	73.04	75.04	79.00	81.00	85.00	84.14	81.00	81.10	85.58	90.68
125 $[kPa]$	74.72	76.72	79.72	81.72	87.14	89.52	86.88	88.54	90.38	95.92
150 $[kPa]$	76.42	78.42	81.42	83.42	88.14	89.92	90.88	91.40	94.14	96.60
175 $[kPa]$	78.08	80.08	83.08	85.08	86.14	89.92	90.88	92.66	96.76	97.28
200 $[kPa]$	78.08	80.08	83.08	85.08	86.14	89.92	90.88	92.66	96.76	97.28
225 $[kPa]$	78.08	80.08	83.08	85.08	86.14	89.92	90.88	92.66	96.76	97.28
250 $[kPa]$	78.08	80.08	83.08	85.08	86.14	89.92	90.88	92.66	96.76	97.28

Table C.4: Primary injection map (part 1)

RPM/MAP	3500	4000	4500	5000	5500	6000	6500	7000	7500	8000
0 $[kPa]$	26.14	26.82	26.82	26.82	26.82	26.82	26.82	26.82	25.12	20.82
20 $[kPa]$	45.48	47.30	47.30	47.30	47.30	47.30	47.30	47.30	45.46	40.84
40 $[kPa]$	67.20	71.24	72.72	72.72	72.72	72.72	72.72	72.72	70.68	65.58
50 $[kPa]$	77.34	78.32	79.98	79.98	79.98	79.98	79.98	79.98	77.98	72.98
60 $[kPa]$	83.78	84.66	84.66	84.66	84.66	84.66	84.66	84.66	82.66	77.66
80 $[kPa]$	87.84	89.18	89.18	89.18	89.18	89.18	89.18	89.18	87.18	82.18
100 $[kPa]$	91.60	91.60	92.54	92.54	92.54	92.54	92.54	92.54	90.54	85.54
125 $[kPa]$	97.60	97.60	97.60	97.60	97.60	97.60	97.60	97.60	95.60	90.60
150 $[kPa]$	98.40	99.14	99.98	101.42	103.12	103.30	102.96	101.98	98.96	93.66
175 $[kPa]$	99.20	98.66	100.76	103.64	106.96	106.84	108.32	106.36	102.34	96.74
200 $[kPa]$	99.20	101.60	104.56	110.28	114.42	114.96	114.90	109.64	104.32	98.62
225 $[kPa]$	99.20	101.60	104.56	110.28	114.42	114.96	114.90	109.64	104.32	98.62
250 $[kPa]$	99.20	101.60	104.56	109.18	114.42	114.96	114.90	109.64	104.32	98.62

Table C.5: Primary injection map (part 2)

C.9 M84 ECU challenges

C.9.1 Oil metering pump management

The M84 ECU is not design to control the OMP. An Arduino system has been programmed (cfr. Figure C.9) to open the OMP valve by using regressions made for each speed depending on table C.1.

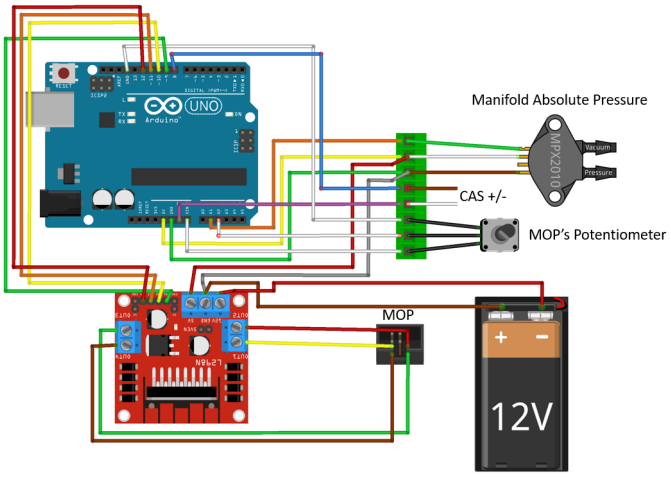

Figure C.9

After setting up the different devices (the stepper motor who pushes linearly a rod to control the opening of the meter oil pump and the crank angle sensor who

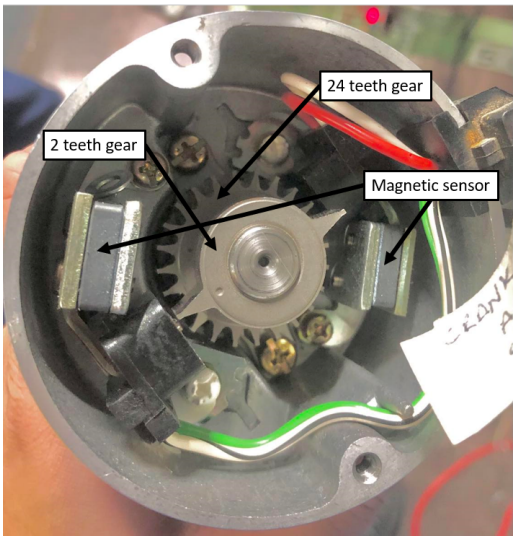

Figure C.10: Crank angle sensor

measures the rotation speed of the engine) the Arduino run a loop constantly. At the beginning, The frequency is measured by the FreqMeasure.h library. The frequency in $[Hz]$ means that there is a certain number of impulsion per second detected. To convert this frequency into rotation speed, the speed has to be measured by the CAS.

By looking at the Figure C.10, there is two sets of gears. One has 24 teeth (used as reference) and the other one 2 (for the synchronisation). Thus, the frequency is from the pulse created by the passing of a teeth in front a the magnetic sensor. The conversion of this frequency response to a rotational speed is dictated by the equation C.2 that is translate in the next part of the Arduino code.

$$\Omega = \frac{60}{24} f \tag{C.2}$$

To read the Manifold Absolute Pressure, the gross value emitted by the sensor needs to be converted into an absolute pressure corresponding to the equation C.3 that is translate in the next part of the Arduino code.

$$p_{abs} = \frac{\frac{p_{brut}}{205} - 2}{2.5} - 0.13 \tag{C.3}$$

Next, the code computes the opening valve value corresponding according to the Table C.1. In consequence, for each rotational speed, there is a regressions (cfr. Figure C.11) where the opening of the MOP depends on the precise value of the pressure.

Finally, the actual percentage of opening of the OMP is given by the OMP's potentiometer. Therefore, depending on the value that the potentiometer send us, the program correct the computed value above and the OMP's position.

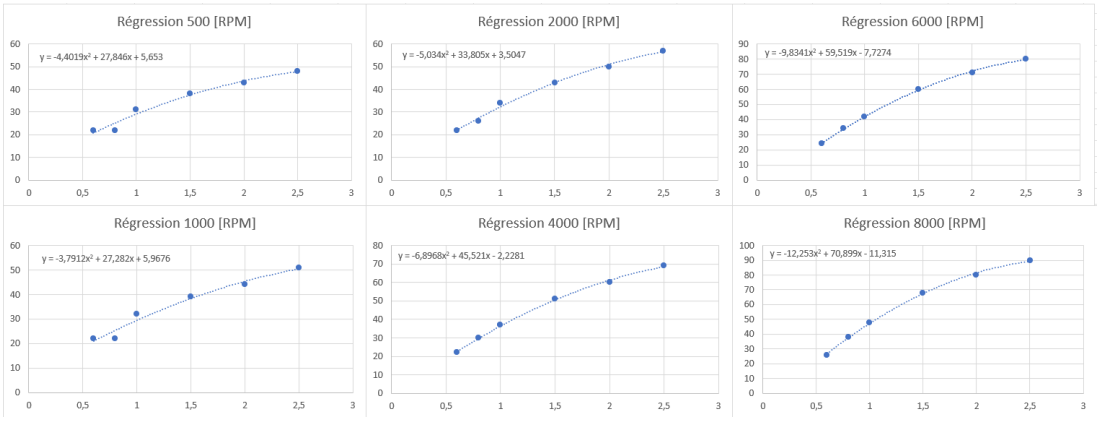

Figure C.11: Regressions

Listing C.1: Arduino code

```
#include <FreqMeasure.h>
#include <Stepper.h>

float rpm ;
float stepsPerRevolution = 58;
Stepper myStepper(stepsPerRevolution, 8, 9, 10, 11);
int cons = 50 ;

void setup() {
  Serial.begin(9600);
  FreqMeasure.begin();

  myStepper.setSpeed(100);
  Serial.begin(9600);
  myStepper.step(stepsPerRevolution);
  delay(500);
}

double sum=0;
int count=0;

void loop() {
```

```
if (FreqMeasure.available()) {
  unsigned long count = FreqMeasure.read();
  float frequency = FreqMeasure.countToFrequency(count)↩
     ;
  float rpm = frequency*60/24;

  float valeur_brute = analogRead(A1);
  float pression_rel = (((valeur_brute/205)-2)/2.5)↩
     -0.13;
  float pression_abs = pression_rel + 1;
  if (rpm < 500){
    cons = (-4.4019*pression_abs*pression_abs) + ↩
       (27.846*pression_abs) + 5.653;
  }
  else if (rpm >= 500 && rpm < 1000){
    cons =  (-3.7912*pression_abs*pression_abs) + ↩
       (27.282*pression_abs) + 5.9676;
  }
  else if (rpm>=1000 && rpm < 2000){
    cons = (-5.034*pression_abs*pression_abs) + ↩
       (33.805*pression_abs) + 3.5047;
  }
  else if (rpm >=2000 && rpm < 4000){
    cons = (-6.8968*pression_abs*pression_abs) + ↩
       (45.521*pression_abs) - 2.2281;
  }
  else if (rpm >= 4000 && rpm < 6000){
    cons = (-9.8341*pression_abs*pression_abs) + ↩
       (59.519*pression_abs) - 7.7274;
  }
  else if (rpm >= 6000 && rpm < 8000){
    cons = (-12.253*pression_abs*pression_abs) + ↩
       (70.899*pression_abs) - 11.315;
  }
  else {
    cons = 100 ;
  }
  float position_brute = analogRead(A2);
  float tension = position_brute * 5 / 1024;
  int position_pourcent = ((-66.66*tension)+200);
```

```
    if (position_pourcent<cons)  {
      myStepper.step(-1);
      delay(25);
    }
    else  {  }
    if (position_pourcent>cons)  {
      myStepper.step(1);
      delay(25);
    }
    else  {  }
    delay(25);
  }
}
```

C.9.2 Throttle body control

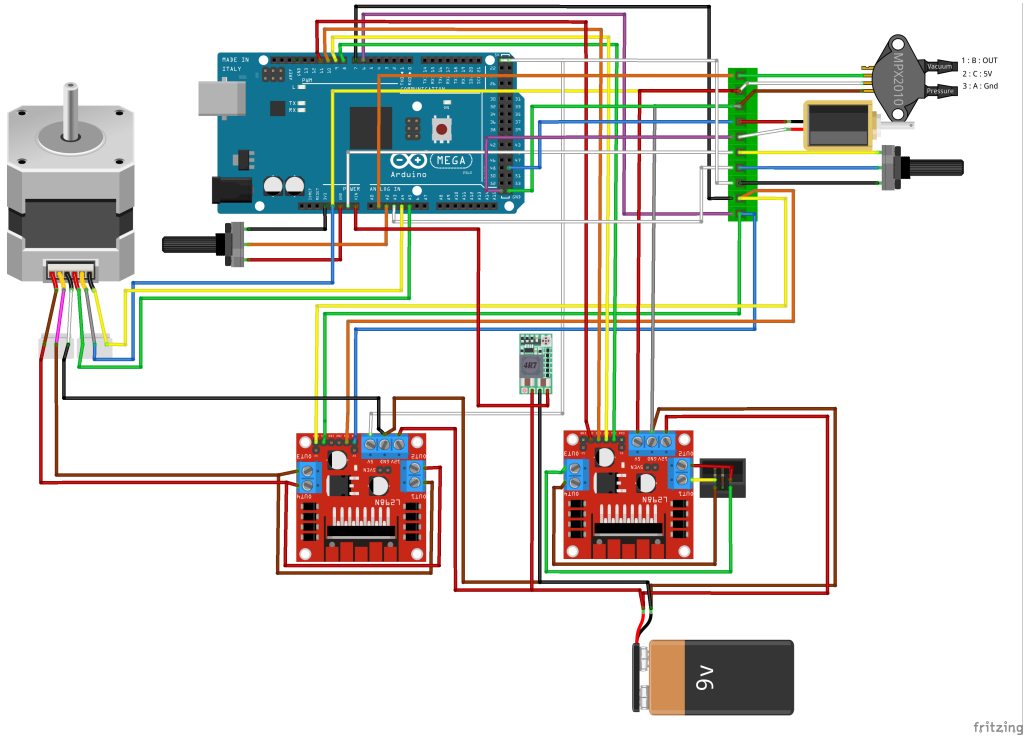

Figure C.12: Arduino full connection including OMP and throttle body control

Listing C.2: Arduino code

```
double E1 = 6;
double M1 = 7;
double E2 = 8;
double M2 = 9;
double value=5;
double potentio = 0;
double pourcent = 0;
motorSpeed= 255

void setup()
{
  pinMode(M2, OUTPUT);
  Serial.begin(9600);
  digitalWrite(M2,LOW);

  analogWrite(enA, motorSpeed);
  analogWrite(enB, motorSpeed);
}

void loop()
{
  //int value=5;
  float TPS1 = analogRead(A3);
  float TPS2 = analogRead(A5);
  potentio = analogRead(A1);

  Serial.print("Valeur analogique : ");
  Serial.println(potentio);
  Serial.println(TPS1);

  potentio = map(potentio,0,1023,0,100);
  Serial.print("Valeur mappee : ");
  Serial.println(potentio);
  pourcent = map(TPS1,135,944,0,100);
  Serial.print("Pourcentage d'ouverture : ");
  Serial.println(pourcent);

  value = map(potentio,0,100,50,135);
  Serial.println(value);
```

```
    if (potentio>=pourcent){
      digitalWrite(M2,HIGH);
      analogWrite(E2, value);

    }
    else{
      digitalWrite(M2,LOW);
      analogWrite(E2, value);
    }
}
```

Appendix D

Artificial intelligence uses

During the writing of this research, ChatGPT AI has been used exclusively as a first-line grammar corrector. All information in this work relies on scientific sources and personal knowledge acquired during internships and my studies.

UNIVERSITÉ CATHOLIQUE DE LOUVAIN
École polytechnique de Louvain
Rue Archimède, 1 bte L6.11.01, 1348 Louvain-la-Neuve, Belgique | **www.uclouvain.be/epl**